

Accurate closed-form model for nonlinear fiber propagation supporting both high and near-zero dispersion regimes

Original

Accurate closed-form model for nonlinear fiber propagation supporting both high and near-zero dispersion regimes / Zefreh, M. R.; Forghieri, F.; Piciaccia, S.; Poggiolini, P.. - In: OPTICS EXPRESS. - ISSN 1094-4087. - ELETTRONICO. - 29:7(2021), pp. 10825-10852. [10.1364/OE.412662]

Availability:

This version is available at: 11583/2948104 since: 2021-12-31T16:37:17Z

Publisher:

Optical Publishing Group

Published

DOI:10.1364/OE.412662

Terms of use:

This article is made available under terms and conditions as specified in the corresponding bibliographic description in the repository

Publisher copyright

Optica Publishing Group (formely OSA) postprint versione editoriale con OAPA (OA Publishing Agreement)

© 2021 Optica Publishing Group. Users may use, reuse, and build upon the article, or use the article for text or data mining, so long as such uses are for non-commercial purposes and appropriate attribution is maintained. All other rights are reserved.

(Article begins on next page)



Accurate closed-form model for nonlinear fiber propagation supporting both high and near-zero dispersion regimes

MAHDI RANJBAR ZEFREH,^{1,*}  FABRIZIO FORGHIERI,² STEFANO PICIACCIA,² AND PIERLUIGI POGGIOLINI¹

¹*DET, Politecnico di Torino, C.so Duca degli Abruzzi 24, 10129 Torino, Italy*

²*Cisco Photonics Italy srl, via Santa Maria Molgora 48/C, 20871 Vimercate (MB), Italy*

**mahdi.ranjbarzefreh@polito.it*

Abstract: Legacy fibers with near-zero and even zero-dispersion bands are being re-purposed worldwide to host modern coherent systems, in the quest to exploit all possible deployed cables. Non-linearity modeling for these legacy fibers has not been investigated in depth and no fast closed-form models are available which are capable of dealing with them. In this work, we first investigate the accuracy of the EGN model for the prediction of the impact of fiber nonlinearity on optical coherent transmission systems at zero or near-zero dispersion. We find the EGN model to be accurate in predicting system performance. We then derive a closed-form EGN-model approximation capable of handling any combination of high, low and near-zero or zero dispersion fibers, which we thoroughly test over 9,000 randomized system scenarios. The good accuracy and real-time computation speed of such a closed-form model potentially makes it a highly flexible tool for supporting physical-layer-aware management of optical networks, capable of dealing with all types of fiber, including legacy ones.

© 2021 Optical Society of America under the terms of the [OSA Open Access Publishing Agreement](#)

1. Introduction

Real-time physical-layer-aware management and optimization of ultra-high-capacity optical networks is becoming an increasingly important aspect of networking, as throughput demand increases. To achieve it, models for fiber non-linear effects (or NLI, Non-Linear-Interference) are needed which must be both accurate and computable in *real-time*.

While several effective NLI models are available [1–7], none of them is real-time in their native form, as they all include numerical integrals. Recently, though, Closed-Form Models (CFMs) that approximate the GN/EGN models have been proposed in [8,9], capable of assessing whole links in fractions of a second. Further improvements and extensions have followed, for instance [10–15].

In [13,14], a machine-learning approach was used to improve the accuracy of the CFMs. In [14] they were tested over 8500 highly randomized system scenarios, showing very good accuracy in reproducing the full-fledged numerically-integrated EGN model, while being many orders of magnitude faster.

However, one limitation of current CFMs is the requirement of fiber dispersion values D being greater than about 2 ps/(nm·km). Below this level, they lose accuracy [14]. The reason why this limitation is significant is that, due to growing traffic demand, there is currently a strong push towards using all available deployed fibers, as well as extending transmission to the L-band wherever possible. While most cables are based on SMF and operate at high dispersion, a considerable portion of deployed cables still hosts non-zero dispersion-shifted fibers (NZDSF), and even legacy dispersion-shifted fibers (DSFs). Both types are low-dispersion across the C and L bands. DSFs typically have a dispersion zero in the C-band and NZDSF typically have a dispersion zero in the L-band. As a result, in the current capacity-constrained scenario, where

there is a strong push towards exploiting all available deployed fiber and all potentially available bands, real-time NLI models for physical layer-aware optical networks must be able to handle near-zero or even zero-dispersion as well.

However, when current CFMs are tested in such low-dispersion scenarios, they show unacceptably high error. In this paper we show this to be the case and try to provide a solution to this problem. We proceeded as follows.

We first tackled the preliminary question of whether the full-fledged numerically-integrated EGN model itself can be considered a reliable tool for performance prediction in low-to-zero dispersion environments. This aspect has never been extensively investigated before, to the best of our knowledge. We tested for this by comparing system performance predictions based on the EGN model with the results of full-band split-step simulations, over 200 randomized systems, where exclusively DSF was present. The results that we found were quite encouraging, as they showed that the EGN model can correctly handle these rather extreme link scenarios as well.

Given the positive results of this preliminary check, we then thoroughly studied the behavior of the best performing among the CFMs proposed in [14], called 'CFM4', over a 600-system randomized test-set, again comprising DSF-only links. While very accurate in reproducing the EGN model when $D > 2$ ps/(nm·km) [14], our extensive investigation confirmed the inadequacy of CFM4 in near-zero or zero-dispersion situations. The investigation also allowed us to identify the main cause of the inaccuracy. It consists of a specific approximation entailing the removal of the so-called Multi-Channel Interference (MCI) [4,16] from the NLI contributions accounted for by the model. This approximation is common to all so far proposed CFMs, as MCI is hard to reduce to closed-form and, at the same time, its contribution to NLI is typically negligible when dispersion is large. However, in low-to-zero dispersion it is necessary to have MCI accounted for as well. So, through extensive calculations, we derived a closed-form approximation for MCI. We then inserted it into CFM4, to produce a new CFM, which we call CFM5.

We then tested CFM5 over the 600-system low-to-zero dispersion test-set as well as over the 8500 links test-set used in [14], for a total of 9100 link configurations. We obtained good overall results. In particular, the error in the 600 near-zero and zero-dispersion links was drastically reduced, while we saw no accuracy degradation of CFM5 with respect to CFM4 on the 8500 conventional links.

Overall, CFM5 is a comprehensive closed-form model capable of approximating the EGN model in all dispersion scenarios, including the challenging near-zero or zero-dispersion links, in real time, with contained error. This potentially makes it a flexible tool for supporting physical-layer-aware management of optical networks, capable of dealing with all types of fiber, including legacy ones.

2. EGN-model accuracy at or near zero-dispersion

The EGN model has been found to be a very accurate tool for the prediction of the amount of NLI impacting coherent transmission systems. However, almost all investigations involving extensive tests and validations of the EGN model have been performed well away from zero dispersion.

To check the EGN-model accuracy and hence its viability for the assessment of NLI in zero or near-zero dispersion scenarios, we first performed a comparison vs. split-step simulations in the case of a very regular and uniform system configuration. We then moved on to more challenging tests based on randomized configurations. These tests are shown in the next two sections.

2.1. Testing the EGN model in a uniform system scenario

We considered an optical link consisting of identical 80 km DSF spans with dispersion zero located at $\lambda_c = 1550$ nm, with dispersion slope $\beta_3 = 0.121$ ps³/km. Loss was $\alpha = 0.22$ dB/km and the nonlinearity coefficient $\gamma = 1.77$ (W·km)⁻¹. The WDM comb consisted of 23 channels with the same launch power, with the center channel placed exactly at frequency of the dispersion

zero. The transmission rate was $R_s = 64$ GBaud and the frequency spacing was $\Delta f = 87.5$ GHz. The channels were raised-cosine shaped with roll-off 0.2. The loss of each span was exactly compensated for by the EDFA placed at the end of the span.

We considered two formats: PM-16QAM and PM-64QAM. The EDFAs noise figure was 5 dB and 6 dB for the PM-64QAM and PM-16QAM systems, respectively. The Channels Under Test (CUTs) were the 1st, 11th, 12th, 13th and 23rd of the comb, as shown in Fig. 1.

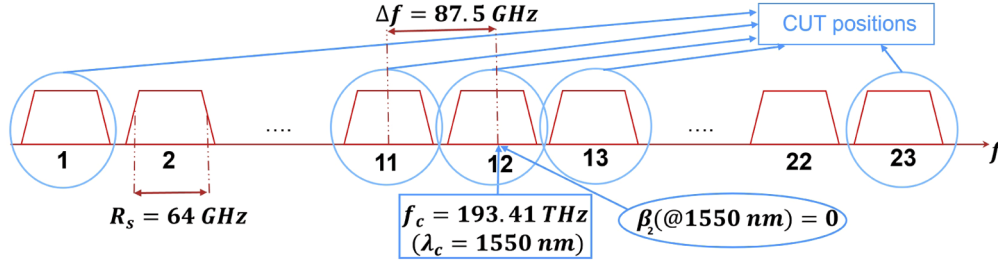


Fig. 1. The WDM comb scheme considered for the first test described in Sect. 2.

In the split-step simulations, max-reach was established based on thresholds related to either GMI or the average SNR directly measured on the received constellation. The GMI max-reach thresholds were chosen as 87% of the constellation entropy, i.e., 6.96 and 10.44 bits/symb for PM-16QAM and PM-64QAM, respectively. In this paper we used [17] Eqs. (31) and (32) to estimate GMI from the constellation. The SNR max-reach thresholds were the ones corresponding to the above GMI values in AWGN, i.e., 11.47 dB for PM-16QAM and 17 dB for PM-64QAM. Note that the receiver used a 2x2 complex LMS equalizer operated initially in training mode, which was then ‘frozen’ to perform the measurements. We tested such receiver simulation software in back-to-back with ASE noise, at the target SNR, and it delivered a performance which was superimposed to the ideal BER vs. SNR curves for all formats, showing to be equivalent to an ideal matched-filter receiver in these conditions.

The simulation-based max-reach assessments were compared with EGN-model max-reach estimates which were obtained by first numerically integrating the full-fledged version of the model [4] to obtain the power spectral density of NLI, $G_{\text{NLI}}(f)$. Then, using Eq. (10) in [14], $G_{\text{NLI}}(f)$ was matched-filtered to find the power of NLI affecting the demodulated constellation (P_{NLI}). Next, P_{NLI} was inserted into the non-linear SNR formula:

$$\text{SNR} = \frac{P_{\text{CUT}} - P_{\text{NLI}}}{P_{\text{ASE}} + P_{\text{NLI}}} \quad (1)$$

where P_{ASE} is the noise power affecting the received constellation due to ASE. Note that this version of the SNR formula approximately accounts for signal-power depletion due to conversion of signal power into NLI, by subtracting P_{NLI} from P_{CUT} at the numerator [18]. Max-reach was then assessed using the same SNR thresholds introduced before.

All the max-reach results are shown in Fig. 2. Interpolation was used to avoid hard quantization of max-reach values to an integer number of spans. As a first remark, the reach of the three center channels is significantly shorter than that of the extreme channels. This was expected, since the extreme channels (1 and 23) operate at a local dispersion $|D| = 0.57$ ps/(nm·km) which, though very low, is not zero, as for the three center channels. In particular, the center channel is especially challenged by operating at *exactly* zero dispersion throughout the link. The other prominent feature of Fig. 2 is that, remarkably, there is very good agreement among the different max-reach prediction methods. In particular, the EGN model max-reach prediction matches quite accurately the ones found through split-step simulations, for all five tested channels. This

represents a quite encouraging first indication of the viability of the EGN model as a performance prediction tool at near-zero or zero dispersion.

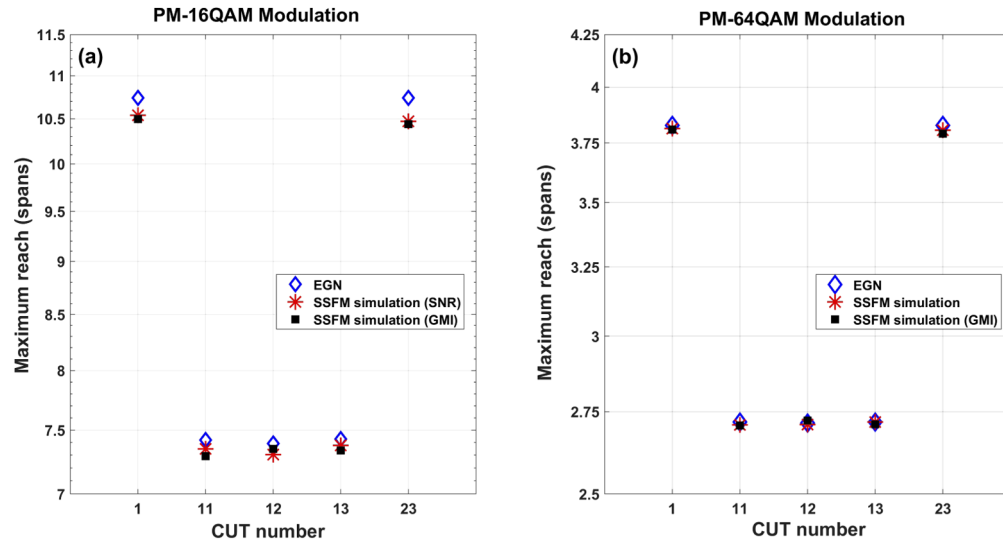


Fig. 2. Maximum reach predictions for different channels-under-test (CUTs) using both the EGN-model and split-step Fourier method (SSFM) simulations. (a): PM-16-QAM. (b): PM-64QAM. The test systems used 23 WDM channels at 64 GBaud, spaced 87.5 GHz, and identical 80-km spans of DSF with dispersion zero located at the center channel (#12) frequency.

As an interesting aside, the max reach assessment through split-step simulations show GMI and SNR-based results to essentially coincide. This is in general not a granted circumstance. While it has been shown to be verified in high-dispersion systems, it had not been shown to hold for near-zero and zero-dispersion ones. Note that the correspondence between SNR and GMI is firmly established, by the well-know laws, only if noise is additive, Gaussian and circular. In the case at hand, at low dispersion, noise could have substantial non-circularity and SNR could be different from constellation point to constellation point, for instance due to some non-linear phase noise. So, there can be, in principle, some discrepancy between the value of reach found based on SNR or based on GMI, even in the case both are directly measured on the constellation. Interestingly, this offset appears quite limited, which is reassuring. This result will be confirmed later on on a much larger sample of systems. However, while it would be interesting to investigate this aspect more in depth, we leave this for possible future investigation.

Overall, these initial tests showed the EGN model to be able to provide accurate performance prediction in the challenging environment of near-zero or even zero-dispersion, at least in the highly regular set-ups used in this first test. Actual networks are however characterized by links that are much less regular and uniform. We therefore proceeded to test the reliability of the EGN model in predicting link performance when many different highly non-uniform randomized test systems are considered.

2.2. Testing the EGN model over a randomized system test-set

Similar to the approach in [13,14], which used a set of randomized scenarios to test the accuracy of various CFMs, we built a test-set consisting of randomly generated full C-band (5 THz) low-dispersion test systems.

The test systems were generated as follows. The WDM comb was centered at 193.41 THz (1550nm). The symbol rate of each individual channel in a comb was randomly chosen among 32, 64, 96 and 128 GBaud with roll-off uniformly-distributed between 0.05 and 0.25. The null-to-null frequency spacing of any two adjacent channels was randomly chosen between 5 and 20 GHz with uniform distribution. The modulation format of each channel was any of PM-QPSK, PM-8QAM, PM-16QAM, PM-32QAM and PM-64QAM. The target SNRs for max-reach were set to correspond to a GMI of 87% of the entropy of each constellation (in AWGN).

The fiber was DSF with $\alpha = 0.22$ dB/km, $\gamma = 1.77$ (W·km)⁻¹ and $\beta_3 = 0.121$ ps³/km. The zero-dispersion wavelength λ_c of each span was randomly chosen with a Gaussian distribution with mean 1550 nm and standard deviation (st-dev) 5 nm. The length of each span was randomized and uniformly distributed between 80 and 120 km. The EDFAs noise figures were selected randomly between 6 and 7 dB. The nominal launch power of each channel was approximately optimized according to the LOGO strategy [3] Eq. (82). The channel under test (CUT) could be any one out of the three center ones, or one of the two extreme channels in the WDM comb, similar to Fig. 1. Note though that, in contrast to Fig. 1, here channels are neither all identical nor equally spaced.

We generated 200 instances of the test links described above and performed full C-band split step simulations for all of them. Following the same methodology used in [14], we compared GMI and SNR values found via either the EGN model or the split-step simulations. This was done to obtain a precise appraisal of the accuracy of the modeling.

In detail, the test procedure was as follows. For each test system, first the max-reach was estimated, using the EGN model, as an integer number of spans. Note that due to the great diversity of the randomized links, the max-reach ranged overall between 1 and 16 spans. Note also that this estimate of the max-reach was used only to set a suitable measuring location for the comparison between the different GMI and SNR estimators. The max-reach itself was not the object of the accuracy test.

At max-reach, the SNR was evaluated both using the EGN-model, according to Eq. (1), yielding SNR_{EGN} , and was also measured on the received constellation obtained through the split-step simulations, providing SNR_{SSS} . We then computed the SNR estimation error as:

$$\Delta_{\text{SNR}}^{\text{dB}} = \text{SNR}_{\text{EGN}}^{\text{dB}} - \text{SNR}_{\text{SSS}}^{\text{dB}} \quad (2)$$

A similar procedure was used for GMI, whose estimation error was computed as:

$$\Delta_{\text{GMI}} = \text{GMI}_{\text{EGN}} - \text{GMI}_{\text{SSS}} \quad (3)$$

Note that GMI cannot be calculated directly from the EGN model. Therefore, to obtain GMI_{EGN} we took SNR_{EGN} and converted it using the ideal SNR-vs.-GMI curves (in AWGN) of the relevant modulation format (see [19] Fig. 8, shown for reference and for the Readers' convenience here in Fig. 3). GMI_{SSS} was instead directly estimated from the simulated received constellation points.

The SNR and GMI errors between EGN-model and split step simulations over the 200-system test-set are shown in Fig. 4, as histograms. The GMI errors Δ_{GMI} are normalized to GMI_{max} , which is the ideal entropy of the modulation format for the channel under test, i.e., 4, 6, 8, 10 and 12 bits/symb for PM-QPSK, PM-8QAM, PM-16QAM, PM-32QAM and PM-64QAM respectively.

The results of Fig. 4 are overall quite encouraging. Across the wide variety of test systems, including CUTs with different positions in the comb, very different symbol rates and different modulation formats, the mean error is less than 0.2 dB, with a standard deviation of only 0.13 dB. Regarding GMI errors, they are in the low single-digit percentage point. Nonetheless, there are some outliers and the histograms of Fig. 4(a) suffer from relatively large peak errors (0.73 dB for SNR and about 5% for GMI).

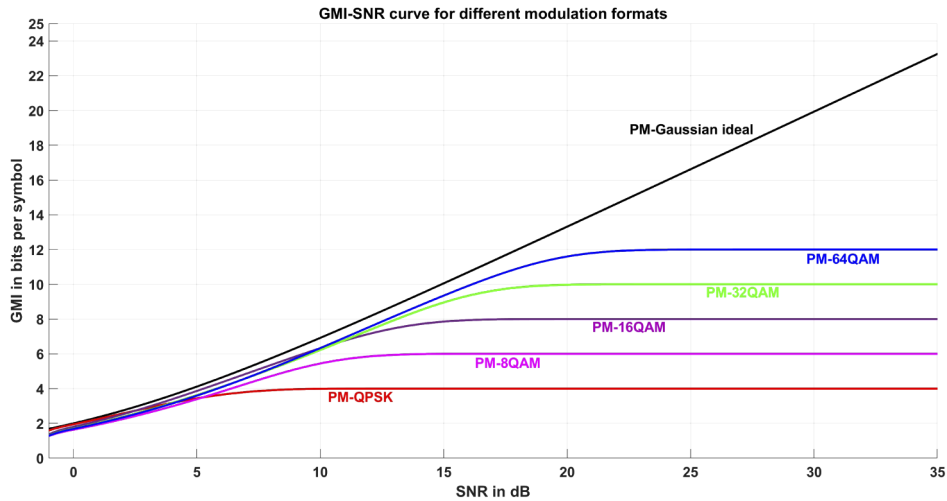


Fig. 3. GMI versus SNR in AWGN for the different modulation formats used in the system test-set. Shannon’s polarization-multiplexed (PM) Gaussian ideal capacity curve is shown for reference [19].

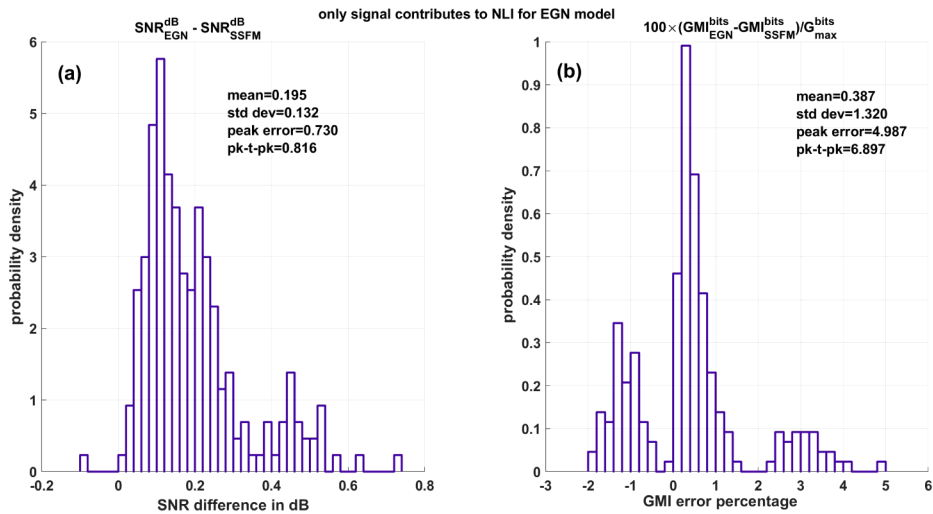


Fig. 4. Histograms of the difference between EGN-model based estimates and split-step simulations measurements. (a): SNR difference, Eq. (2). (b): GMI difference, Eq. (3). ASE noise is *not* considered in the NLI estimation based on the EGN model.

When we looked at the data points that have a larger error, we found out that most of them correspond to CUTs using either PM-QPSK or PM-8QAM. These CUTs operate at low SNR, which entails that the ASE noise power is relatively large with respect to the signal power. In these conditions, ASE is large enough to produce significant NLI itself, especially for PM-QPSK. Therefore, we decided to re-assess the EGN-model results considering not only signal but also ASE in the generation of NLI. While a rigorous estimation of the generation of NLI due to ASE is possible [20,21], we used a simple *approximate* approach, similar to what was proposed in [18]: in the EGN model calculations of NLI we added the in-band P_{ASE} to the power of each channel, updating it at the start of each span. Note that while being heuristic, this approach has a physical justification: the power that would be measured for each channel in an actual system, at any point in the link, would indeed coincide with our ‘ASE-corrected’ value. On the other hand, certain aspects are neglected. For instance, the two EGN model parameters Φ and Ψ [see [4], Eqs. (6)], that depend on the statistical moments of the constellation points, are altered by adding ASE noise and should be corrected. While doable in principle, we neglect this correction in this paper.

The results with such approximate approach for ASE-generated NLI are shown in Fig. 5. The errors, both for SNR and GMI, are substantially decreased in all statistical indicators. However, both plots still show a somewhat bi-modal profile, with a secondary lower peak to the left of the primary one. We looked at the CUTs making up the lower side peaks and found *all* of them to be PM-8QAM CUTs. We found no immediately evident explanation of this circumstance and, since the extra error for these PM-8QAM systems is modest (about 0.2 dB SNR and 2% GMI), we decided to proceed and leave this aspect for future investigation.

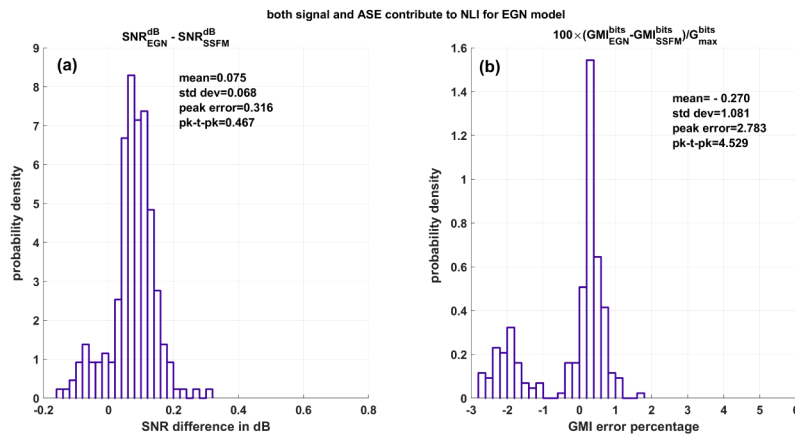


Fig. 5. Histograms of the difference between EGN-model estimates and split-step simulations measurements. (a): SNR difference. (b): GMI difference. The generation of NLI due to ASE noise is approximately accounted for in the NLI calculations based on the EGN-model.

In conclusion, we can state that the EGN model performs quite well in predicting system performance even at near-zero or zero dispersion, to within an error that should be sufficient for the vast majority of practical use scenarios. However, the EGN model is orders of magnitudes slower than needed for real-time applications. In the next sections we will try to obtain a real-time CFM that approximates well the EGN model even in challenging near-zero or zero-dispersion conditions.

3. Accuracy of closed-form models for NLI evaluation at or near zero-dispersion

In this section we investigate the accuracy of the real-time CFMs presented in [14] when used in a near-zero or zero-dispersion environment. Specifically, we focus on the most accurate of

them, called CFM4 in [14]. It was derived from the CFM Eq. (41) in [3], by upgrading it to support frequency-dependent dispersion and attenuation. In addition, CFM4 makes use of machine-learning to improve its ability to reproduce the EGN model results faithfully. Specifically, two simple ‘correction factors’, called $\rho_{nch}^{(n)}$ and $\rho_{cut}^{(n)}$ in [14], were added to CFM4 and trained over a large training set of system scenarios. CFM4 was then tested over a test-set, for the most part different from the training set, made up of 8500 randomized systems, achieving the best accuracy among the CFMs proposed in [14], with SNR estimation error mean and standard deviation both below 0.1 dB (vs. the EGN model).

However, as mentioned in the introduction, the key requirement to obtain such good accuracy is that $D > 2$ ps/(nm·km). Below this level, key approximations used to obtain CFM4 (as well as the other CFMs in [14]) from the EGN model break down. So, we expected CFM4 to be inadequate at lower dispersion. Nonetheless, to establish a reference, we tested CFM4 over a near-zero and zero-dispersion system test-set generated according to the description of Sect. 2.2, this time comprising 600 system.

The test procedure was similar to the one described in Sect. 2.2. Again, for each test system, the max-reach was estimated as an integer number of spans using the EGN-model. At such max-reach, the SNR was evaluated, according to Eq. (1), both using the EGN-model and CFM4, yielding SNR_{EGN} and SNR_{CFM} , respectively. We then computed the SNR estimation error as:

$$\Delta_{SNR}^{dB} = SNR_{CFM}^{dB} - SNR_{EGN}^{dB} \quad (4)$$

The error histogram over the 600-system test-set are depicted in Fig. 6. It is evident that CFM4 does not work satisfactorily for near-zero dispersion systems. The error standard deviation for CFM4 is 0.59 and its peak value is 2.68 dB, which are clearly unacceptable levels for reliable modeling. In passing, we mention that we also tested CFM1 through CFM3 from [14], obtaining comparable (CFM2 and CFM3) or worse (CFM1) results vs. CFM4.

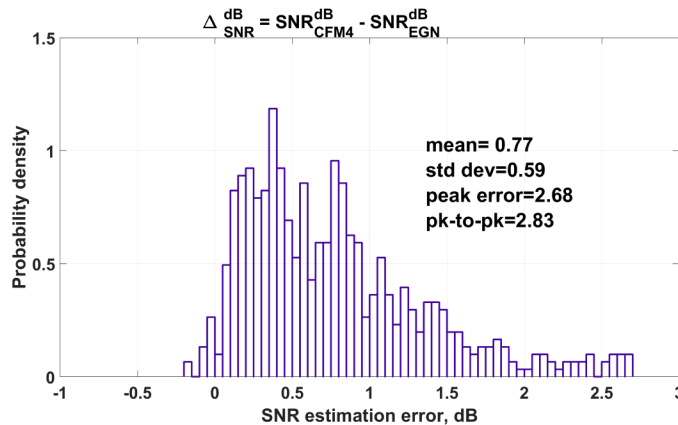


Fig. 6. Histogram of the SNR estimation error between CFM4 and the EGN model, over the 600-system near-zero and zero-dispersion test-set generated according to the description of Sect. 2.2.

We then investigated the possible causes. The seemingly most likely reason behind the inaccuracy of the CFMs [14] at very low dispersion is that they were derived under the assumption that the ‘multi-channel interference’ (MCI, [4]) contributions to NLI in the GN/EGN model integrals are negligible. As a rule of thumb, for most systems MCI starts being non-negligible when the mentioned dispersion threshold $D < 2$ ps/(nm·km) is reached. As dispersion gets lower, the discrepancy between the CFMs and the EGN-model prediction increases. This appears to match the behavior shown by the CFMs. Also, neglecting the MCI contributions to NLI means

estimating less total NLI than the EGN model, which can be expected to result in a higher predicted SNR than the EGN model. Indeed, the histogram of Fig. 6 is skewed towards the right, i.e., towards higher SNRs. This appears to further confirm the conjecture that it is the lack of the MCI terms that causes the inaccuracy.

One possible objection to some of the reasoning proposed above is the following. As mentioned, CFM4 relies in part on ‘machine learning’ to improve its accuracy and deliver the very good results shown in [14]. So, perhaps the unsatisfactory result of Fig. 6 is due to lack of training on the specific near-zero or zero-dispersion systems that CFM4 is now used on. To rule out this possibility, we actually re-trained CFM4 while adding a substantial amount of near-zero and zero-dispersion systems to the training set. The result will be commented in depth in Sect. 5. We can already say though that the re-training could not improve the performance of CFM4.

4. Extending the closed-form models to account for MCI contributions

As shown in the previous section, our analysis suggests that neglecting MCI is the likely cause for the substantial discrepancy between CFM4 from [14] and the EGN model when dispersion is at or near zero. In this section we start over from the description of the system modeling premises and assumptions in order to gradually arrive at the derivation of the multi-channel interference (MCI) contributions which are missing in the CFMs.

To present the derivation of the MCI contributions, we first have to establish some conventions and notation. The structure of the coherent WDM optical fiber communication systems that we want to model in this paper is as follows. They are composed of N_s fiber spans. A typical fiber span is shown in Fig. 7. Between two adjacent fiber spans, an optical amplification element is assumed. We assume that the input signal propagates along the \hat{z} direction in the fiber span. The length of n_s -th fiber span is $L_s(n_s)$ and can be different span by span. The input signal, which is denoted by $E_{in}(f)$ in frequency domain, enters the fiber span at $z = 0$. In the absence of nonlinearity, i.e. $\gamma_{n_s} = 0$, the electrical field propagates along z as $E(z, f) = E_{in}(f) \times \exp(-jz\beta_{n_s}(f) - \alpha_{n_s}(f)z)$ where $\alpha_{n_s}(f)$ and $\beta_{n_s}(f)$ are the fiber attenuation and propagation coefficients, respectively. These two quantities can be in general frequency-dependent and can be different span by span, hence the subscript n_s . The propagation coefficient is customarily characterized by a Taylor series as:

$$\beta_{n_s}(f) = \beta_{0,n_s} + 2\pi\beta_{1,n_s}(f - f_{n_s}^c) + \frac{4\pi^2}{2}\beta_{2,n_s}(f - f_{n_s}^c)^2 + \frac{8\pi^3}{6}\beta_{3,n_s}(f - f_{n_s}^c)^3 \quad (5)$$

where β_{0,n_s} , β_{1,n_s} , β_{2,n_s} and β_{3,n_s} are four constants with respect to frequency. $f_{n_s}^c$ is the center frequency for the Taylor expansion and is a constant for each span.

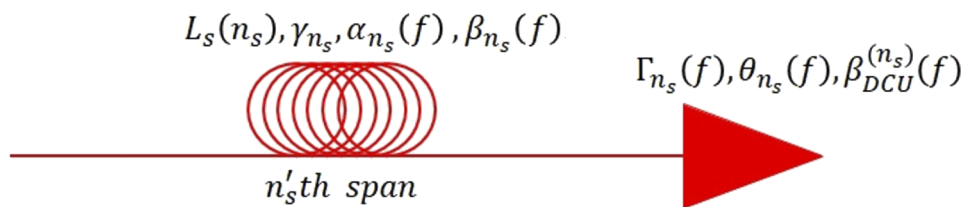


Fig. 7. A typical fiber span in the system.

The attenuation coefficient $\alpha_{n_s}(f)$ is assumed to be a slowly varying function with respect to frequency, so that it can be approximated with a constant over each WDM channel, while it can be different channel by channel in the WDM comb. Therefore, the total power attenuation of the n_s -th span (due to signal propagation from $z = 0$ up to $z = L_s(n_s)$), in the absence of nonlinearity,

is:

$$A_{n_s}(f) = \exp(-2\alpha_{n_s}(f) L_s(n_s)) \quad (6)$$

The amplification element shown in Fig. 7 is assumed to potentially comprise an actual amplifier (such as an EDFA), a spectral shaping filter (including a frequency-dependent phase factor) and a dispersion compensating element. It is modeled as a Linear Time Invariant (LTI) system whose input-output electrical field relation in frequency domain, neglecting the noise of the amplifier, is:

$$E_{\text{out,amp}}(f) = E_{\text{in,amp}}(f) \times \sqrt{\Gamma_{n_s}(f)} \times \exp(j\theta_{n_s}(f)) \times \exp(-j\beta_{\text{DCU}}^{(n_s)}(f)) \quad (7)$$

where $\Gamma_{n_s}(f)$, $\theta_{n_s}(f)$ are the power gain and the phase shift due to the amplifier and filter, and are considered slowly-varying functions with respect to frequency. They are approximated as constants over each WDM channel, but may be different channel by channel. The parameter $\beta_{\text{DCU}}^{(n_s)}(f)$ describes a dispersion compensating element, if present. Note that the amplification element input-output *power* relation, neglecting the noise of the amplifier, is:

$$P_{\text{out,amp}}(f) = |E_{\text{out,amp}}(f)|^2 = |E_{\text{in,amp}}(f)|^2 \times \Gamma_{n_s}(f) = P_{\text{in,amp}}(f) \times \Gamma_{n_s}(f) \quad (8)$$

The power spectral density (PSD) of the nonlinear interference (NLI) based on the general formula of the GN model is [3,22]:

$$G_{\text{NLI}}(f) = \frac{16}{27} \times \int_{-\infty}^{+\infty} \int_{-\infty}^{+\infty} G_s(f_1) \times G_s(f_2) \times G_s(f_1 + f_2 - f) \times |LK(f_1, f_2, f_1 + f_2 - f)|^2 df_1 df_2 \quad (9)$$

where in Eq. (9), $G_s(f)$ is the power spectral density (PSD) of the WDM signal launched into the fiber and $LK(\cdot)$ is the link function which is determined based on the fiber link configuration and will be discussed later. The WDM PSD can be written in terms of each channel PSD as:

$$G_s(f) = \sum_{m_{\text{ch}}=1}^{N_c} G_{m_{\text{ch}}}(f) \quad (10)$$

where N_c is the number of channels in the WDM comb and $G_{m_{\text{ch}}}(f)$ is the PSD of the m_{ch} -th channel in the WDM comb. Combining Eq. (9) and Eq. (10) we have:

$$G_{\text{NLI}}(f) = \frac{16}{27} \times \sum_{m_{\text{ch}}=1}^{N_c} \sum_{n_{\text{ch}}=1}^{N_c} \sum_{k_{\text{ch}}=1}^{N_c} \int_{-\infty}^{+\infty} \int_{-\infty}^{+\infty} G_{m_{\text{ch}}}(f_1) \times G_{n_{\text{ch}}}(f_2) \times G_{k_{\text{ch}}}(f_1 + f_2 - f) \times |LK(f_1, f_2, f_1 + f_2 - f)|^2 df_1 df_2 \quad (11)$$

We then concentrate on the CUT and look at its center frequency, i.e., f_{CUT} . The PSD of NLI at f_{CUT} is given by:

$$G_{\text{NLI}}(f_{\text{CUT}}) = \frac{16}{27} \times \sum_{m_{\text{ch}}=1}^{N_c} \sum_{n_{\text{ch}}=1}^{N_c} \sum_{k_{\text{ch}}=1}^{N_c} \int_{-\infty}^{+\infty} \int_{-\infty}^{+\infty} G_{m_{\text{ch}}}(f_1) \times G_{n_{\text{ch}}}(f_2) \times G_{k_{\text{ch}}}(f_1 + f_2 - f_{\text{CUT}}) \times |LK(f_1, f_2, f_1 + f_2 - f_{\text{CUT}})|^2 df_1 df_2 \quad (12)$$

We assume that the PSD of each channel in the WDM comb is raised-cosine. For now, we approximately replace it with a rectangular channel with the same center frequency as the original raised-cosine channel. Also, we assume that the null-to-null bandwidth of the approximate rectangular channel is equal to the symbol rate (baud rate) of the original raised cosine channel.

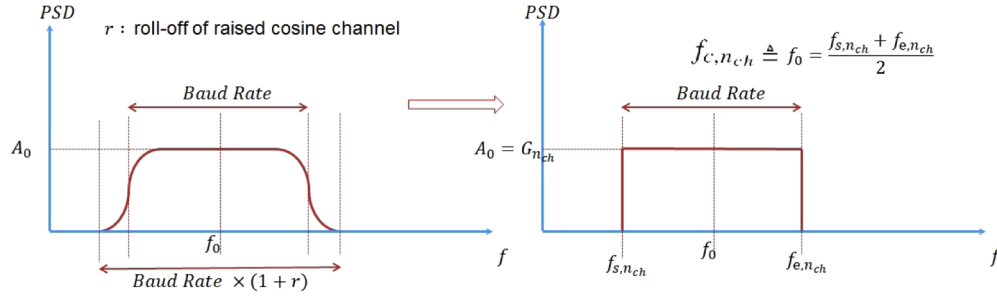


Fig. 8. Approximating the PSD of a raised-cosine channel with a rectangular PSD.

We set the flat-top value of the rectangular PSD to the same value as that of the flat-top of the PSD of the original raised-cosine channel, as it is shown in Fig. 8.

In Fig. 8, r and f_0 are the roll-off and center frequency of the original raised-cosine channel, respectively. Also, $f_{s,n_{ch}}$ and $f_{e,n_{ch}}$ are the ‘start’ (low) and ‘end’ (high) frequency edges of the rectangular channel, respectively. We also define: $f_{c,n_{ch}} \triangleq \frac{f_{s,n_{ch}} + f_{e,n_{ch}}}{2}$, as the center frequency of the n_{ch} -th channel. The center frequency of the CUT is: $f_{c,CUT} \triangleq f_{c,CUT} = \frac{f_{s,CUT} + f_{e,CUT}}{2}$. Applying the rectangular PSD approximation to Eq. (11) we can rewrite it as:

$$G_{NLI}(f_{CUT}) = \frac{16}{27} \times \sum_{m_{ch}=1}^{N_c} \sum_{n_{ch}=1}^{N_c} \sum_{k_{ch}=1}^{N_c} G_{m_{ch}} \times G_{n_{ch}} \times \int_{f_{s,n_{ch}}}^{f_{e,n_{ch}}} \int_{f_{s,m_{ch}}}^{f_{e,m_{ch}}} G_{k_{ch}}(f_1 + f_2 - f_{CUT}) \times |LK(f_1, f_2, f_1 + f_2 - f_{CUT})|^2 df_1 df_2 \quad (13)$$

where $G_{m_{ch}}$ in Eq. (13) is $G_{m_{ch}} \triangleq P_{m_{ch}}/R_{m_{ch}}$ where $P_{m_{ch}}$ and $R_{m_{ch}}$ are the power at the launch location and the Baud rate of the channel m_{ch} , respectively. Equation (13) can then be rewritten as:

$$G_{NLI}(f_{CUT}) = \frac{16}{27} \times \sum_{m_{ch}=1}^{N_c} \sum_{n_{ch}=1}^{N_c} \sum_{k_{ch}=1}^{N_c} G_{m_{ch}} \times G_{n_{ch}} \times G_{k_{ch}} \times \iint_{S_{m_{ch},n_{ch},k_{ch}}} |LK(f_1, f_2, f_1 + f_2 - f_{CUT})|^2 df_1 df_2 \quad (14)$$

The double integral in Eq. (14) must be carried out over certain confined domains in the $f_1 - f_2$ plane, i.e. $S_{m_{ch},n_{ch},k_{ch}}$, which are defined as shown below:

$$S_{m_{ch},n_{ch},k_{ch}} = \left\{ f_1 \in \mathbb{R}, f_2 \in \mathbb{R} \mid f_{s,m_{ch}} \leq f_1 \leq f_{e,m_{ch}} \ \& \ f_{s,n_{ch}} \leq f_2 \leq f_{e,n_{ch}} \ \& \ f'_{s,k_{ch}} \triangleq f_{s,k_{ch}} + f_{CUT} \leq f_1 + f_2 \leq f_{e,k_{ch}} + f_{CUT} \triangleq f'_{e,k_{ch}} \right\} \quad (15)$$

We call such confined domains *integration islands*, as originally done in [16]. In Fig. 9 we can see the formation of a typical integration island in the $f_1 - f_2$ plane, hatched in blue color.

Each integration island generates an additive contribution to the total NLI impinging on the CUT. Specifically, the island $S_{m_{ch},n_{ch},k_{ch}}$ represents the NLI, created by the non-linear interaction of the WDM channels of index m_{ch} , n_{ch} and k_{ch} , which falls within the bandwidth of the CUT. Note that indices may repeat and that one or more of the indices can be that of the CUT.

The shape of each island may be rather different based on the bandwidth and spacing of the channels involved. Also, not all combinations of the three indices correspond to an actual island. In fact, while any combination of indices may be fed to Eq. (15), many of such combinations result in an ‘empty island’ (zero-area), which therefore generates no additional NLI. This does

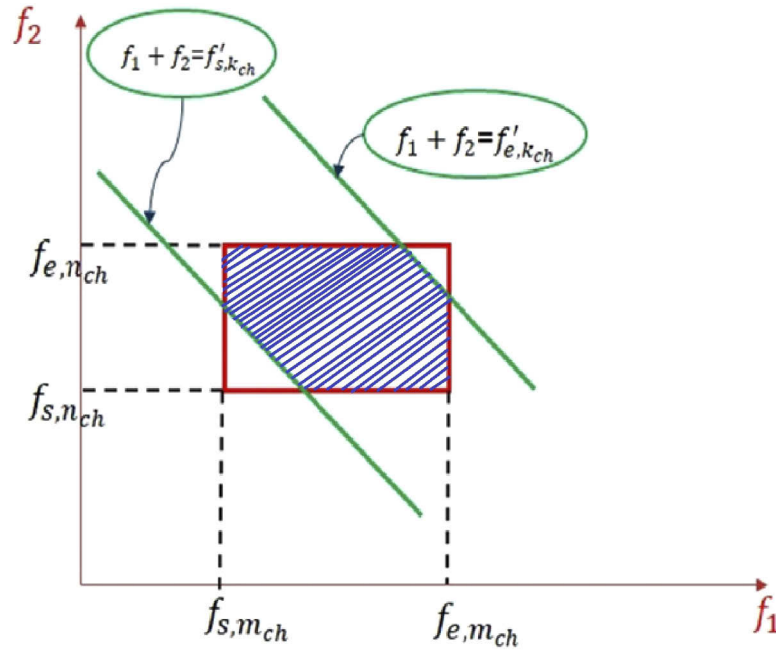


Fig. 9. Formation of a typical integration island based on the criteria mentioned in Eq. (15).

not mean that the three channels do not interact non-linearly: rather, it means that the non-linear interaction of the three channels falls outside of the bandwidth of the CUT and therefore does not affect it.

We define the set $S^{(\text{islands})}$ as the set of all possible integration islands:

$$S^{(\text{islands})} \triangleq \left\{ S_{m_{ch},n_{ch},k_{ch}} \mid m_{ch} \in \mathbb{N}, n_{ch} \in \mathbb{N}, k_{ch} \in \mathbb{N}, \right. \\ \left. 1 \leq m_{ch} \leq N_c, 1 \leq n_{ch} \leq N_c, 1 \leq k_{ch} \leq N_c \right\} \quad (16)$$

Using Eq. (16), Eq. (14) can be re-written as:

$$G_{\text{NLI}}(f_{\text{CUT}}) = \frac{16}{27} \times \sum_{\{S_{m_{ch},n_{ch},k_{ch}} \in S^{(\text{islands})}\}} G_{m_{ch}} \times G_{n_{ch}} \times G_{k_{ch}} \times \\ \iint_{S_{m_{ch},n_{ch},k_{ch}}} |LK(f_1, f_2, f_1 + f_2 - f_{\text{CUT}})|^2 df_1 df_2 \quad (17)$$

The set $S^{(\text{islands})}$ can be written as the union of two sets: $S^{(\text{islands})} = S_1^{(\text{islands})} \cup S_2^{(\text{islands})}$, where the two sets are disjoint: $S_1^{(\text{islands})} \cap S_2^{(\text{islands})} = \emptyset$. They are defined as:

$$S_1^{(\text{islands})} \triangleq \left\{ S_{m_{ch},n_{ch},k_{ch}} \in S^{(\text{islands})} \mid (m_{ch} = \text{CUT} \ \& \ n_{ch} = k_{ch}) \text{ or } (n_{ch} = \text{CUT} \ \& \ m_{ch} = k_{ch}) \right\} \\ S_2^{(\text{islands})} \triangleq \left\{ S_{m_{ch},n_{ch},k_{ch}} \in S^{(\text{islands})} \mid S_{m_{ch},n_{ch},k_{ch}} \notin S_1^{(\text{islands})} \right\} \quad (18)$$

Therefore, $G_{\text{NLI}}(f_{\text{CUT}})$ can be written as:

$$G_{\text{NLI}}(f_{\text{CUT}}) = G_{\text{NLI}}^{(1)}(f_{\text{CUT}}) + G_{\text{NLI}}^{(2)}(f_{\text{CUT}}) \quad (19)$$

where $G_{\text{NLI}}^{(1)}(f_{\text{CUT}})$ and $G_{\text{NLI}}^{(2)}(f_{\text{CUT}})$ are:

$$G_{\text{NLI}}^{(1)}(f_{\text{CUT}}) \triangleq \frac{16}{27} \times \sum_{\{S_{m_{\text{ch}}, n_{\text{ch}}, k_{\text{ch}}} \in S_1^{(\text{islands})}\}} G_{m_{\text{ch}}} \times G_{n_{\text{ch}}} \times G_{k_{\text{ch}}} \times \iint_{S_{m_{\text{ch}}, n_{\text{ch}}, k_{\text{ch}}}} |LK(f_1, f_2, f_1 + f_2 - f_{\text{CUT}})|^2 df_1 df_2 \quad (20)$$

$$G_{\text{NLI}}^{(2)}(f_{\text{CUT}}) \triangleq \frac{16}{27} \times \sum_{\{S_{m_{\text{ch}}, n_{\text{ch}}, k_{\text{ch}}} \in S_2^{(\text{islands})}\}} G_{m_{\text{ch}}} \times G_{n_{\text{ch}}} \times G_{k_{\text{ch}}} \times \iint_{S_{m_{\text{ch}}, n_{\text{ch}}, k_{\text{ch}}}} |LK(f_1, f_2, f_1 + f_2 - f_{\text{CUT}})|^2 df_1 df_2 \quad (21)$$

In the derivation of CFM1-CFM4 in [14], the key approximation of $G_{\text{NLI}}^{(2)}(f_{\text{CUT}}) \cong 0$ was made. In other terms: $G_{\text{NLI}}(f_{\text{CUT}}) \cong G_{\text{NLI}}^{(1)}(f_{\text{CUT}})$. The rationale behind this approximation is that whenever dispersion is not too close to zero, the contribution of the islands in S_2 becomes small and they can be neglected [4] Fig. 3, [22]. This aspect was recognized and used early on, for instance to derive CFM [3], Eq. (42), called CFM0 in [14], of which CFM1-CFM4 represent extensions and generalizations. The circumstance that the islands in S_2 could be neglected was quite welcome, since accounting for them in closed-form proves significantly more difficult than for the islands in S_1 .

The set of islands S_2 roughly corresponds to the set of the so-called MCI islands (see [4,16]), i.e., to the set of islands that involve three different WDM channels (no repetition in the three indices m_{ch} , n_{ch} and k_{ch}). This is why neglecting the S_2 islands can also be termed as ‘neglecting MCI’. For reference, the islands in S_1 include the so-called SCI and XCI-X1 islands [22]. However, as shown in Sect. 3, Fig. 6, neglecting MCI for zero and near zero dispersion scenarios causes considerable error in the NLI calculation. Therefore, to be able to deal with these scenarios, one needs to take into account the MCI contribution too, that is $G_{\text{NLI}}^{(2)}(f_{\text{CUT}})$ needs to be accounted for in the NLI evaluation. It is worth mentioning that the islands in S_1 consist of those that account for the traditional taxonomy ‘cross-phase modulation’ (XPM) effect, as well as self-phase modulation (SPM), the latter consisting of a single island. The islands in S_2 can roughly be ascribed to four-wave mixing (FWM).

To include the $G_{\text{NLI}}^{(2)}(f_{\text{CUT}})$ contribution in the NLI assessment, we first replace each complex-shaped integration island from S_2 with a suitable rectangular-shaped approximation of it. This is done in Appendix A. Then, in Appendix B, the double NLI integral Eq. (21) is calculated in closed-form for each of the rectangular islands, leading to a closed-form expression for the whole $G_{\text{NLI}}^{(2)}(f_{\text{CUT}})$ contribution.

5. Accuracy assessment of the augmented closed form model CFM5

In the previous sections we used the closed-form model CFM4 exactly as it was defined in [14]. In particular, the 24 free parameters $a_1 - a_{24}$ that appear in the machine-learning-based ‘correction factors’ $\rho_{n_{\text{ch}}}^{(n)}$ and $\rho_{\text{CUT}}^{(n)}$, which had been ‘trained’ in [14], were left unchanged.

We then added the analytical MCI term $G_{\text{NLI}}^{(2)}(f_{\text{CUT}})$ to obtain CFM5. The model has therefore changed and it makes sense that the corrections factors be re-trained. It also makes sense that, for a fair comparison, also the corrections factors of CFM4 be re-trained, giving it perhaps a chance to improve on the poor results shown in Fig. 6. Note that we want the CFMs to be effective on *both* near-zero dispersion systems *and* on the widely diverse but more conventional systems considered in [14]. As a consequence, the training set must now comprise suitable samples of both the systems addressed in [14] and the near-zero and zero-dispersion systems addressed here, as well.

Training was hence done for both CFM4 and CFM5 over a total of 600 training systems, of which 300 were randomly selected from the test-set of 8,500 C-band links described in [14] and 300 were randomly selected among the zero-inline dispersion links specified in Sect. 2.2. The training procedure is otherwise the same as described in Sect. V of [14]. The new optimized parameters $a_1 - a_{24}$ for CFM5 are shown in Table 1.

Table 1. Optimized values of the parameters $a_1 - a_{24}$ for the machine-learning factors of CFM5

parameter	value	parameter	value
a_1	+1.0529e0	a_{13}	+9.9806e-9
a_2	-6.3717e-1	a_{14}	-1.111e0
a_3	+9.2990e-1	a_{15}	+5.9989e-3
a_4	-2.5140e0	a_{16}	+5.0878e+5
a_5	+6.5246e-1	a_{17}	+3.1832e+3
a_6	-1.0680e0	a_{18}	-2.1131e0
a_7	+4.4556e-29	a_{19}	+1.1485e-1
a_8	+2.3111e-3	a_{20}	+4.0594e+2
a_9	+8.7048e-1	a_{21}	-2.9537e-1
a_{10}	-1.7748e0	a_{22}	+2.9319e-1
a_{11}	+2.2391e-2	a_{23}	-1.2452e0
a_{12}	-1.7977e+1	a_{24}	+1.8435e0

The histograms of the SNR estimation error for the re-trained CFM4 and for CFM5 are shown in Figs. 10 and 11. To see how they perform in the various system configurations, four plots are shown in both figures. Plots (a) are results over the the same 600 zero-inline dispersion test-set defined in Sect. 2.2 where it was used to test the (non-retrained) CFM4 histogram shown in Fig. 6.

Comparing Fig. 10(a) with Fig. 6, i.e., non-retrained with re-trained CFM4, we can see that even with re-training CFM4 still performs poorly over the zero-inline dispersion test-set. Improvements are marginal and the histogram is still quite substantially spread out.

Looking now at CFM5 performance over the zero-inline dispersion test-set, Fig. 11(a), we can see an overall much better behavior vs. both the non-retrained CFM4 of Fig. 6 and the re-trained CFM4 of Fig. 10(a). Taking the latter as reference, the peak error of CFM5 is much smaller, 0.85 dB vs. 2.13 dB. The mean error is virtually zero for CFM5 and the standard deviation shrinks by 60% vs. CFM4, scoring a quite contained value of 0.22 dB.

This good result would however be of limited use if CFM5 was not accurate over more conventional systems. We therefore tested CFM5 over the same 8,500 highly-randomized system test-set presented in [14], where CFM4 performed very well. In short, the set includes all QAM modulation formats from QPSK to 256QAM, as well as Gaussian-shaped constellations. Three different fiber types are randomly intermixed in the links (SMF, E-LEAF, TWC). Symbol rates range from 32 to 128 GBaud and many other parameters are also randomized. Please see [14] for all details and parameter values.

Remarkably, Figs. 11(b), 11(c), and 11(d), which show the error histograms for the lowest, middle and highest frequency channels in the combs, indicate that the performance of CFM5 is quite good. Incidentally, the reason why the histogram for the highest-frequency channel Fig. 11(d) is somewhat worse than the other two channels Figs. 11(b), 11(c), is that the TWC fiber spans, present in some of the systems of the test-set, had dispersion at that frequency of only about $D=0.6$ ps/(nm·km), making such spans near-zero dispersion and hence more challenging.

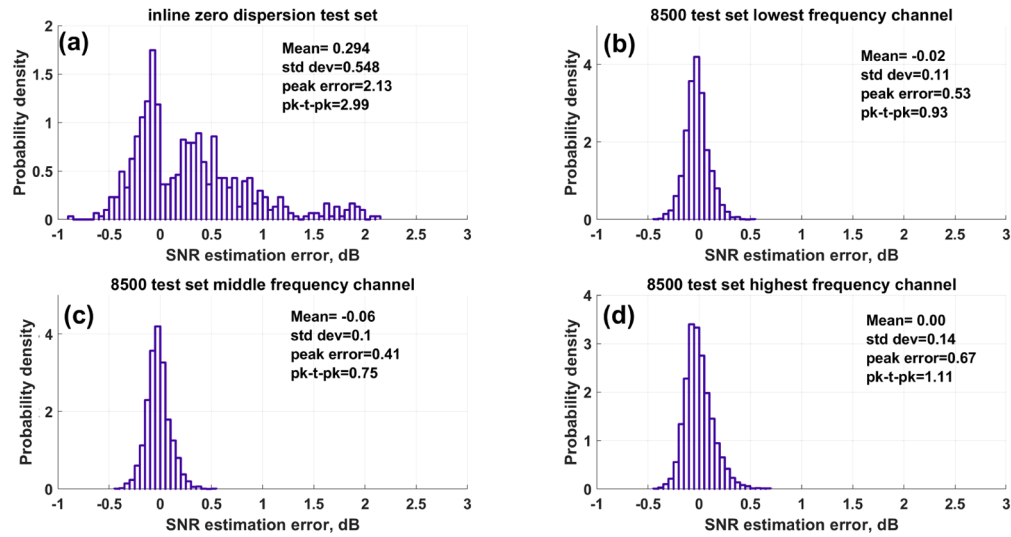


Fig. 10. Histogram of the SNR estimation error between CFM4 and EGN model where the machine-learning correction terms are re-trained using a training set that combines both near-zero and zero-dispersion systems, with conventional systems from [14]. (a): zero in-line dispersion test set; (b): lowest frequency channel for the 8500-system test set from [14]; (c): middle frequency channel for the 8500-system test set from [14]; (d): highest frequency channel for the 8500-system test set from [14].

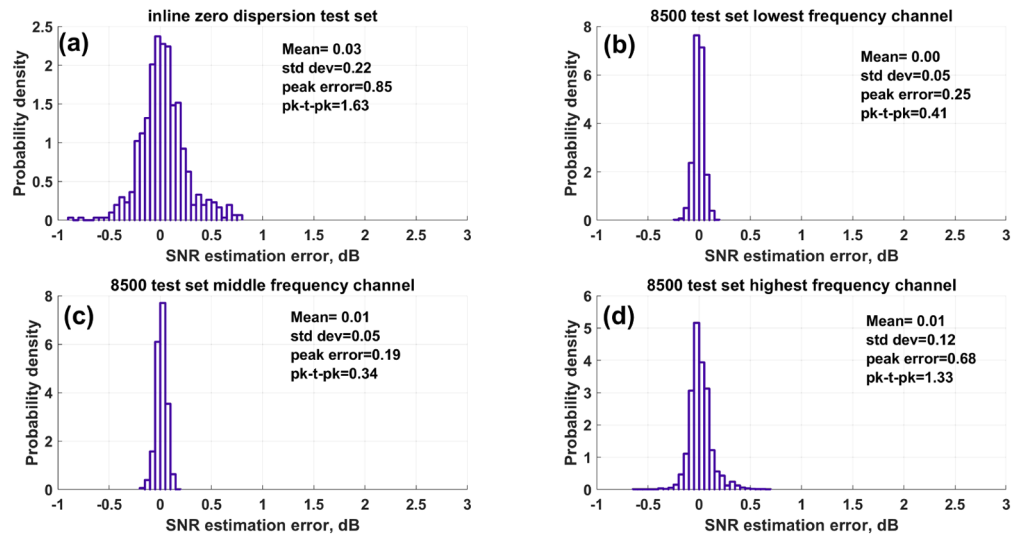


Fig. 11. Histogram of the SNR estimation error between CFM5 and EGN model where the machine-learning correction terms are re-trained using a training set that combines both near-zero and zero-dispersion systems, with conventional systems from [14]. (a): zero in-line dispersion test set; (b): lowest frequency channel for the 8500-system test set from [14]; (c): middle frequency channel for the 8500-system test set from [14]; (d): highest frequency channel for the 8500-system test set from [14].

In any case, a comparison with the corresponding plots for CFM4 from [14] shows that CFM5 performs almost the *same* as CFM4 over the 8,500 systems test-set of [14], for which CFM4 had been trained.

Instead, the corresponding plots for CFM4 *after re-training* including the near-zero and zero dispersion systems, Figs. 10(b), 10(c), and 10(d), are actually substantially worse than both CFM5 and non-retrained CFM4 [14]. This result quite strikingly shows that trying to force CFM4 to support near-zero and zero-dispersion systems by training it over these systems too, not only does not produce improvements over these systems, but actually degrades substantially CFM4 accuracy over the systems of the 8,500 systems test-set [14]. This strongly hints at CFM4 simply not being analytically equipped to deal with near-zero and zero-dispersion systems.

In contrast CFM5, thanks to the added MCI contribution $G_{\text{NLI}}^{(2)}(f_{\text{CUT}})$, manages to achieve a good performance over near-zero and zero-dispersion systems while retaining a very good performance over more conventional systems.

As a final comment, while representing very substantial improvement, Fig. 11 does show that the accuracy of CFM5 for near-zero and zero-dispersion systems is clearly still not as good as for conventional systems. This is due to the very challenging nature of near-zero and zero-dispersion systems, where NLI generation calls into play complex-shaped EGN-model ‘islands’ over which closed-form integration is difficult and can only be carried out with approximations (see Appendices A and B).

On the other hand, the achieved results may be acceptable in many practical situations and CFM5 could in those cases be a very useful real-time tool for carrying out on-the-fly management and control or optimization of systems and networks.

6. CFM5 vs. split-step simulations

So far our benchmark in the evaluation of the accuracy of the CFMs has been the EGN model. This made sense since we know that the EGN model is quite accurate, as discussed before. We also specifically tested the accuracy of the EGN model in near-zero and zero-dispersion in Sect. 2, with quite positive outcome.

Nonetheless, we decided to perform a direct comparison between split-step simulations and CFM5, since the former are arguably the ultimate benchmark (short of validation experiments, which however typically pose difficult hurdles). The limitation in this case is the number of systems that can be practically considered, due to the computational effort required by simulations. We considered 200 systems, randomly selected out of the 600 zero-dispersion scenarios described in Sect. 2.2. We looked at both SNR and generalized mutual information (GMI), similarly to what was done in Sect. 2.2 when comparing the EGN model vs. split-step simulations. We did it again at max-reach, at a GMI which is 87% of the entropy of the constellation. Note that for SNR estimation with CFM5 we used again Eq. (1) and we also approximately took into account NLI generated by ASE noise, as explained in Sect. 2.2.

Figure 12 shows the error histograms for SNR and GMI between CFM5 and split step simulations. The GMI error is normalized by GMI_{max} which is the maximum GMI of the modulation format for the channel under test, i.e. 4, 6, 8, 10 and 12 bits/symb for PM-QPSK, PM-8QAM, PM-16QAM, PM-32QAM and PM-64QAM respectively.

We consider the results quite positive. Specifically, there appears to be no substantial degradation vs. the most directly comparable result, i.e., the SNR error histogram of Fig. 11(a). The standard deviation is the same. Peak error indicators are even lower in Fig. 12(a), likely because the the lower number of samples simply did not manage to generate enough outliers. Overall, though, the two histograms are quite comparable and this represents a confirmation of the effectiveness of CFM5.

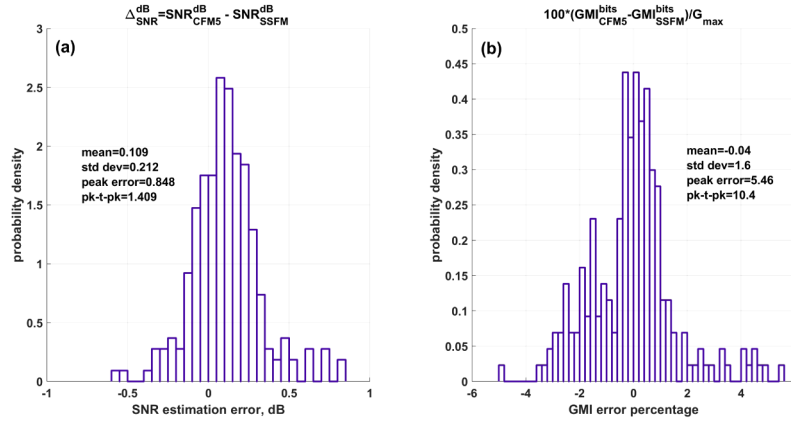


Fig. 12. histogram of the difference between CFM5 and split-step simulations. (a): SNR. (b): GMI.

7. Computation time

As one may expect, by adding $G_{\text{NLI}}^{(2)}(f_{\text{CUT}})$ contribution, the computation time increase. We tested it on the 600 zero-dispersion test-set for CFM4 and CFM5 on a laptop using interpreted MATLAB code. For CFM4 it took 110 seconds to calculate SNR for all 600 systems and for all WDM channels in each system. The same calculation took 1500 seconds for CFM5. The average channel number in each scenario is 48 and average fiber span number is 13. Therefore, we can say that CFM5 is more than one order of magnitude slower than CFM4 due to adding the $G_{\text{NLI}}^{(2)}(f_{\text{CUT}})$ contribution. However, as compared to the EGN model and split-step simulations, CFM5 is still much faster. We ran some extensive tests (370 systems) and found that the speed gap is at least four orders of magnitude in favor of CFM5 vs. EGN.

8. Conclusion

Due to the so-called ‘capacity crunch’, low and even zero-dispersion fibers are being considered for use or re-use. Also, alternative fiber bands are being explored, which can be near or at zero dispersion. In this paper we first tackle the question of whether the EGN model can be considered a reliable tool for performance prediction in such low-to-zero dispersion scenarios. Then, we improve the closed-form model CFM4 from [14] with new analytical terms that make it capable of handling such environments. We finally test it both at low-to-zero dispersion, and over the general test-set used in [14], for a total of over 9,000 system configurations. The good accuracy results show it to potentially be a viable tool for real-time management of physical-layer-aware networks even in challenging low-dispersion scenarios.

Appendix A: approximation of integration islands

To achieve a closed form formula for $G_{\text{NLI}}^{(2)}(f_{\text{CUT}})$ the double integral in Eq. (11) needs to be analytically calculated. One main challenge in calculation of the double integral is the complex shape of the area (integration island) that integral must be calculated over it. In fact, the diversity of the integration island shapes makes the integral solution in Eq. (11) very complex particularly when our approach is finding a closed form formula for the 2-D integral. In Fig. 13 we see some of the possible geometric shapes of integration islands hatched by blue color we may face in a WDM comb scheme.

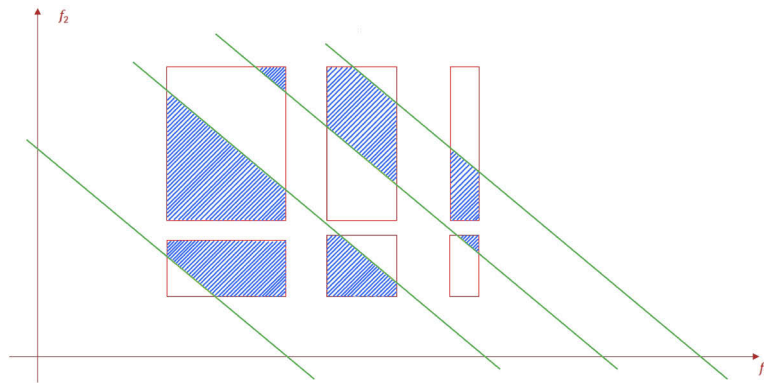


Fig. 13. Some possible shapes for integration islands.

To overcome the problem of complex integration island shapes, our idea is that we find the geometric center of the integration island and then replace the original shape island with a rectangle whose area and geometric center are the same as the original shape. This would be the same as the moment matching approach in the approximation of a 2-D shape with another one in which their three lowest order moments are matched [23]. One example is schematically depicted in Fig. 14 where the red island S_2 is replaced by the blue rectangle island S_1 . Given the said procedure, we expected the result of the integration over the rectangle to be approximately the same as the result of the integration over the original integration island. In the end, though, the only way to validate this approximation was by extensive numerical testing, as we actually did in this paper.

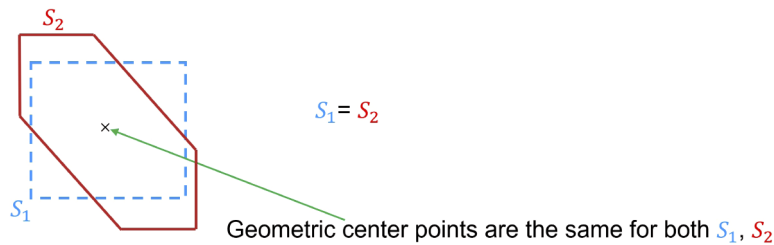


Fig. 14. Replacing an arbitrary shape integration island with a concentric equivalent rectangle with the same area.

Considering S as a set of points in two dimensional $x - y$ plane, the coordinates of the geometric center of S are (x^*, y^*) where:

$$x^* = \frac{\iint_S x dx dy}{\iint_S dx dy}, \quad y^* = \frac{\iint_S y dx dy}{\iint_S dx dy} \quad (22)$$

In detail, the geometric center (centroid) of a parallelogram and a right-angled triangle are shown in Fig. 15 [24]. Furthermore, there are properties for the geometric center calculation. One important property that we use in this appendix is that for a complex shape composed by different sub-shapes, knowing the area and geometric center of each sub-shape, we can easily find the geometric center of the overall combined shape [25] as it is shown in Fig. 16. In general if we have a shape containing N sub-shapes:

$$S = \bigcup_{k=1}^N S_k \quad (23)$$

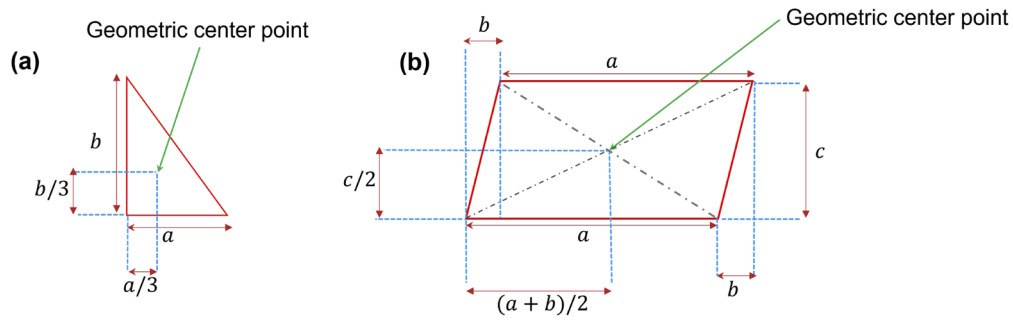


Fig. 15. Geometric center points of (a). a typical right-angled triangle and (b). a typical parallelogram.

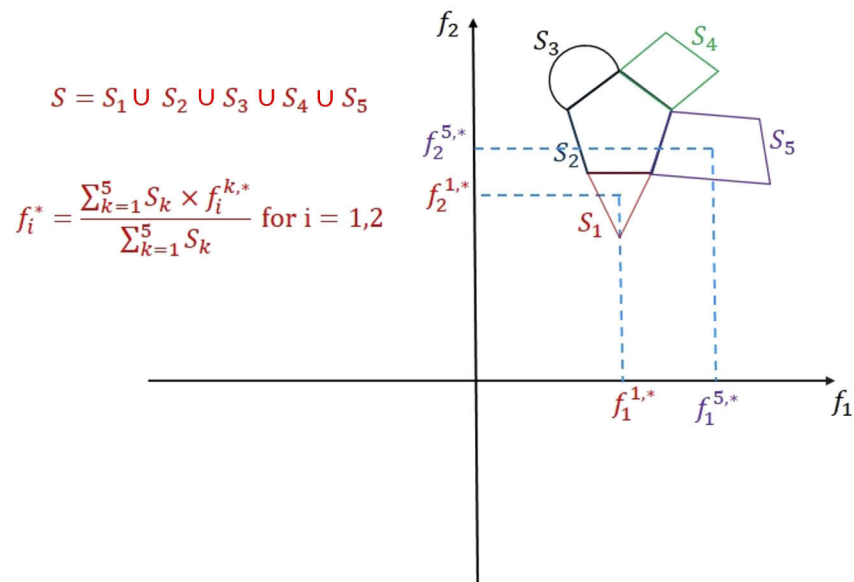


Fig. 16. Geometric center of an overall shape S made up of several sub shapes. The coordinates of the geometric center of sub shape S_k are $(f_1^{k,*}, f_2^{k,*})$ and the coordinates of the geometric center of the overall shape S are (f_1^*, f_2^*) in $f_1 - f_2$ plane.

While we use notations S and S_k both for the shapes (as a set of points in the $f_1 - f_2$ plane) and the area of the shapes, it is also assumed $(f_1^{k,*}, f_2^{k,*})$ to be the coordinates of the geometric center of the sub-shape S_k and (f_1^*, f_2^*) to be the coordinates of the geometric center of the overall shape S . The coordinates of the overall shape are:

$$f_i^* = \frac{\sum_{k=1}^N S_k \times f_i^{k,*}}{\sum_{k=1}^N S_k}, \quad i = 1, 2 \quad (24)$$

On the contrary, if the area and geometric center of the complex shape, composed by different sub shapes, is known and also the area and geometric center of the all the sub shapes except one of them (q-th) are known, by using Eqs. (23) and (24) it is deduced for the sub shape with

unknown geometric center:

$$S_q = S - \bigcup_{k=1, k \neq q}^N S_k \tag{25}$$

$$f_i^{q,*} = \frac{S \times f_i^* - \sum_{k=1, k \neq q}^N S_k \times f_i^{k,*}}{S - \sum_{k=1, k \neq q}^N S_k}, \quad i = 1, 2 \tag{26}$$

These properties are useful in derivation of the geometric center of an arbitrary shape integration island. In general, if we have three basic typical shape geometric center, we will be able to compute the geometric center of an arbitrary island. These general shapes are shown in Fig. 17.

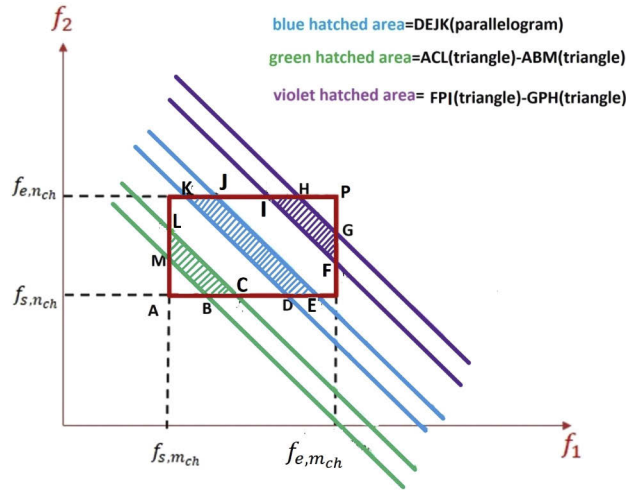


Fig. 17. Three different general shapes forming an arbitrary island.

As it is clear from Fig. 13, each integration island can generally partitioned to the sum of three hatched typical shapes in Fig. 17. In other words, having the geometric center and area of three hatched areas in Fig. 17, we can analytically find geometric center and area of each arbitrary integration island shape by using Eqs. (23), (24), (25) and (26). The area and coordinates of the geometric center of each of the three typical shapes are calculable by considering geometric centers of two geometric shapes, i.e. right-angled triangle and parallelogram shown in Fig. 15(a) and Fig. 15(b) respectively. The green and violet hatched areas in Fig. 17 are the subtraction of two right-angled triangle and also the blue hatched area in Fig. 17 is a parallelogram. Thereupon, the area and geometric center of each of the three basic hatched shapes in Fig. 17 can be calculated by having the geometric center and area of four different typical shapes shown and calculated in Fig. 18.

The area and geometric center of the hatched triangle in Fig. 18(a) are:

$$S_1(\tau) \triangleq \frac{(\tau - f_{s,mch} - f_{s,nch})^2}{2}$$

$$f_1^{(1)}(\tau) \triangleq \frac{2f_{s,mch}}{3} + \frac{\tau}{3} - \frac{f_{s,nch}}{3} \tag{27}$$

$$f_2^{(1)}(\tau) \triangleq \frac{2f_{s,nch}}{3} + \frac{\tau}{3} - \frac{f_{s,mch}}{3}$$

To continue, we first define:

$$BW_{mch} \triangleq f_{e,mch} - f_{s,mch} \tag{28}$$

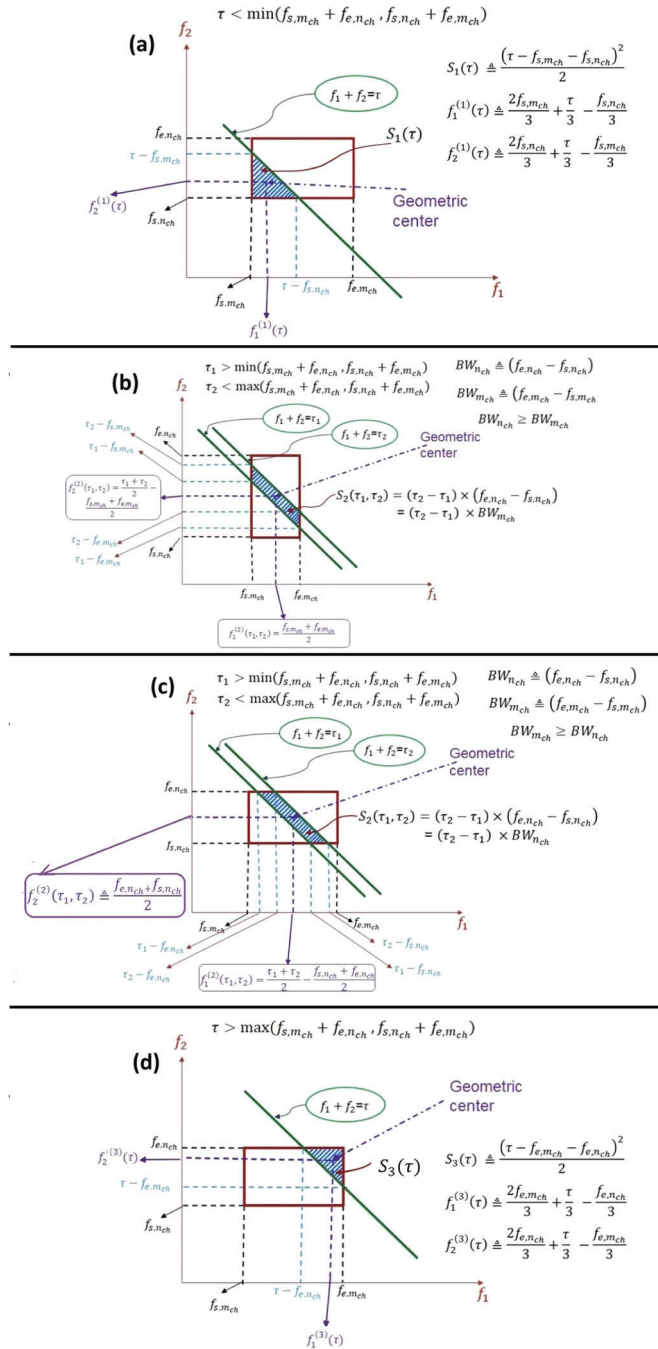


Fig. 18. Four useful typical shapes for modeling an arbitrary integration island.

$$BW_{n_{ch}} \triangleq f_{e,n_{ch}} - f_{s,n_{ch}} \tag{29}$$

$$u(x) \triangleq \begin{cases} 1 & x > 0 \\ \frac{1}{2} & x = 0 \\ 0 & x < 0 \end{cases} \tag{30}$$

We can then easily combine the calculated results in Figs. 18(b) and 18(c) to calculate the hatched parallelogram for two different scenarios $BW_{m_{ch}} > BW_{n_{ch}}$ and $BW_{m_{ch}} < BW_{n_{ch}}$ as:

$$\begin{aligned} S_2(\tau_1, \tau_2) &\triangleq (\tau_2 - \tau_1) \times \min(BW_{m_{ch}}, BW_{n_{ch}}) \\ f_1^{(2)}(\tau_1, \tau_2) &\triangleq \frac{f_{s,m_{ch}} + f_{e,m_{ch}}}{2} \times u(BW_{n_{ch}} - BW_{m_{ch}}) + \\ &\quad \left(\frac{\tau_2 + \tau_1}{2} - \frac{f_{s,n_{ch}} + f_{e,n_{ch}}}{2} \right) \times u(BW_{m_{ch}} - BW_{n_{ch}}) \\ f_2^{(2)}(\tau_1, \tau_2) &\triangleq \frac{f_{s,n_{ch}} + f_{e,n_{ch}}}{2} \times u(BW_{m_{ch}} - BW_{n_{ch}}) + \\ &\quad \left(\frac{\tau_2 + \tau_1}{2} - \frac{f_{s,m_{ch}} + f_{e,m_{ch}}}{2} \right) \times u(BW_{n_{ch}} - BW_{m_{ch}}) \end{aligned} \tag{31}$$

Also the area and geometric center of the hatched triangle in Fig. 18(d) are:

$$\begin{aligned} S_3(\tau) &\triangleq \frac{(\tau - f_{e,m_{ch}} - f_{e,n_{ch}})^2}{2} \\ f_1^{(3)}(\tau) &\triangleq \frac{2f_{e,m_{ch}}}{3} + \frac{\tau}{3} - \frac{f_{e,n_{ch}}}{3} \\ f_2^{(3)}(\tau) &\triangleq \frac{2f_{e,n_{ch}}}{3} + \frac{\tau}{3} - \frac{f_{e,m_{ch}}}{3} \end{aligned} \tag{32}$$

Therefore, we define:

$$f'_{s,k_{ch}} \triangleq f_{s,k_{ch}} + f_{CUT} \tag{33}$$

$$f'_{e,k_{ch}} \triangleq f_{e,k_{ch}} + f_{CUT} \tag{34}$$

$$F_1 \triangleq f_{s,m_{ch}} + f_{s,n_{ch}} \tag{35}$$

$$F_2 \triangleq \min(\{f_{s,m_{ch}} + f_{e,n_{ch}}\}, \{f_{e,m_{ch}} + f_{s,n_{ch}}\}) \tag{36}$$

$$F_3 \triangleq \max(\{f_{s,m_{ch}} + f_{e,n_{ch}}\}, \{f_{e,m_{ch}} + f_{s,n_{ch}}\}) \tag{37}$$

$$F_4 \triangleq f_{e,m_{ch}} + f_{e,n_{ch}} \tag{38}$$

$$\tau_1^+ \triangleq \min(f'_{e,k_{ch}}, F_2) \tag{39}$$

$$\tau_1^- \triangleq \min(f'_{s,k_{ch}}, F_1) \tag{40}$$

$$\tau_1 \triangleq \min(f'_{e,k_{ch}}, F_3) \tag{41}$$

$$\tau_2 \triangleq \min(f'_{e,k_{ch}}, F_2) \tag{42}$$

$$\tau_3^+ \triangleq \max(f'_{s,k_{ch}}, F_3) \tag{43}$$

$$\tau_3^- \triangleq \min(f'_{e,k_{ch}}, F_4) \tag{44}$$

$$S_1^+ \triangleq S_1(\tau_1^+) \times u(F_2 - f'_{s,k_{ch}}) \times u(f'_{e,k_{ch}} - F_1) \tag{45}$$

$$S_1^- \triangleq S_1(\tau_1^-) \times u(F_2 - f'_{s,k_{ch}}) \times u(f'_{e,k_{ch}} - F_1) \tag{46}$$

$$S_2^+ \triangleq S_2(\tau_1, \tau_2) \times u(F_3 - f'_{s,kch}) \times u(f'_{e,kch} - F_2) \quad (47)$$

$$S_3^+ \triangleq S_3(\tau_3^+) \times u(F_4 - f'_{s,kch}) \times u(f'_{e,kch} - F_3) \quad (48)$$

$$S_3^- \triangleq S_3(\tau_3^-) \times u(F_4 - f'_{s,kch}) \times u(f'_{e,kch} - F_3) \quad (49)$$

With above definitions, the area of the integration island is calculated as:

$$S = S_1^+ - S_1^- + S_2^+ + S_3^+ - S_3^- \quad (50)$$

Also the coordinates of the geometric center of the integration island, which we call it (f_1^*, f_2^*) in $f_1 - f_2$ plane, will be:

$$f_1^* \triangleq \frac{S_1^+ \times f_1^{(1)}(\tau_1^+) - S_1^- \times f_1^{(1)}(\tau_1^-) + S_2^+ \times f_1^{(2)}(\tau_1, \tau_2) + S_3^+ \times f_1^{(3)}(\tau_3^+) - S_3^- \times f_1^{(3)}(\tau_3^-)}{S_1^+ - S_1^- + S_2^+ + S_3^+ - S_3^-} \quad (51)$$

$$f_2^* \triangleq \frac{S_1^+ \times f_2^{(1)}(\tau_1^+) - S_1^- \times f_2^{(1)}(\tau_1^-) + S_2^+ \times f_2^{(2)}(\tau_1, \tau_2) + S_3^+ \times f_2^{(3)}(\tau_3^+) - S_3^- \times f_2^{(3)}(\tau_3^-)}{S_1^+ - S_1^- + S_2^+ + S_3^+ - S_3^-} \quad (52)$$

We have another degree of freedom in specifying the ratio between the equivalent rectangle length and width. We simply consider the same value for length and width which indeed the equivalent shape will be a square. Therefore:

$$L_1 = L_2 = \sqrt{S} = \sqrt{S_1^+ - S_1^- + S_2^+ + S_3^+ - S_3^-} \quad (53)$$

It is worth mentioning that making the rectangular shape assumption for the equivalent island was done for simplicity. It is possible that better approximations can be found in future research.

The original integration island and the equivalent rectangle with their coordinates in axis f_1 and f_2 are shown in the Fig. 19.

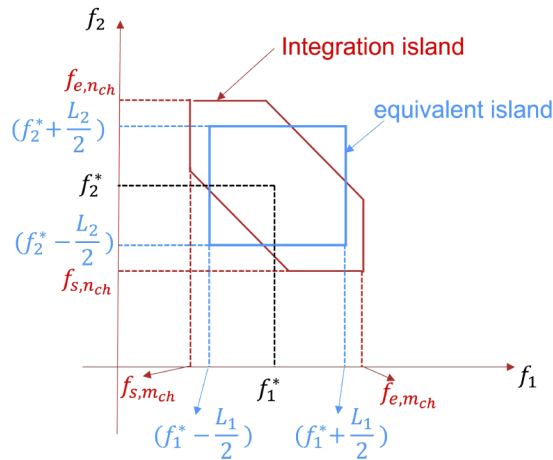


Fig. 19. Original integration island and the equivalent island.

Appendix B: closed form formula derivation

In this Appendix we use the result of Appendix A to find the analytic form of $G_{NL}^{(2)}(f_{cut})$ in Eq. (21). The $LK(\cdot)$ in Eq. (21) is the link function that is specified based on the fiber

link configuration [9,26]. Neglecting Inter-channel Stimulated Raman Scattering (ISRS) and accepting the incoherent GN (iGN) approximation and some other reasonable assumptions, $|LK(f_1, f_2, f_1 + f_2 - f_{\text{CUT}})|^2$ presented in Eq. (14) can be approximated as [9]:

$$\begin{aligned} |LK(f_1, f_2, f_1 + f_2 - f_{\text{CUT}})|^2 &\cong \sum_{n_s=1}^{N_s} \gamma_{n_s}^2 \times \\ &\prod_{p=1}^{(n_s-1)} \Gamma_p(f_{c,m_{\text{ch}}}) \Gamma_p(f_{c,n_{\text{ch}}}) \Gamma_p(f_{k_{\text{ch}}}) A_p(f_{c,m_{\text{ch}}}) A_p(f_{c,n_{\text{ch}}}) A_p(f_{c,k_{\text{ch}}}) \times \\ &\frac{1}{4 \left[\alpha_{n_s}^{(m_{\text{ch}}, n_{\text{ch}}, k_{\text{ch}})} \right]^2 + 16\pi^4 (f_1 - f_{\text{CUT}})^2 (f_2 - f_{\text{CUT}})^2 \times [\beta_{2,n_s} + \pi\beta_{3,n_s} (f_1 + f_2 - 2f_{n_s}^c)]^2} \times \\ &\prod_{p=n_s}^{N_s} \Gamma_p(f_{\text{CUT}}) A_p(f_{\text{CUT}}) \end{aligned} \quad (54)$$

where $\alpha_{(m_{\text{ch}}, n_{\text{ch}}, k_{\text{ch}})}^{(n_s)}$ is defined as [9]:

$$\alpha_{(m_{\text{ch}}, n_{\text{ch}}, k_{\text{ch}})}^{(n_s)} = \frac{\alpha_{n_s}(f_{c,m_{\text{ch}}}) + \alpha_{n_s}(f_{c,n_{\text{ch}}}) + \alpha_{n_s}(f_{c,k_{\text{ch}}}) - \alpha_{n_s}(f_{\text{CUT}})}{2} \quad (55)$$

Now, we use the result of Appendix A and replace the $S_{m_{\text{ch}}, n_{\text{ch}}, k_{\text{ch}}}$ in Eq. (21) with the equivalent rectangular shape. Therefore, Eq. (21) is approximated as:

$$\begin{aligned} G_{\text{NLI}}^{(2)}(f_{\text{CUT}}) &\cong \frac{16}{27} \times \sum_{(m_{\text{ch}}, n_{\text{ch}}, k_{\text{ch}}) \in S'_2} G_{m_{\text{ch}}} \times G_{n_{\text{ch}}} \times G_{k_{\text{ch}}} \times \\ &\int_{f_1^* - L_1/2}^{f_1^* + L_1/2} \int_{f_2^* - L_2/2}^{f_2^* + L_2/2} |LK(f_1, f_2, f_1 + f_2 - f_{\text{CUT}})|^2 df_2 df_1 \end{aligned} \quad (56)$$

where the set S'_2 in Eq. (56) is:

$$\begin{aligned} S'_2 &\triangleq \left\{ (m_{\text{ch}}, n_{\text{ch}}, k_{\text{ch}}) \mid m_{\text{ch}} \in \mathbb{N} \ \& \ n_{\text{ch}} \in \mathbb{N} \ \& \ k_{\text{ch}} \in \mathbb{N} \ \& \right. \\ &1 \leq m_{\text{ch}} \leq N_c \ \& \ 1 \leq n_{\text{ch}} \leq N_c \ \& \ 1 \leq k_{\text{ch}} \leq N_c \\ &\left. \ \& \ (m_{\text{ch}}, n_{\text{ch}}, k_{\text{ch}}) \notin \left\{ (m_{\text{ch}} = \text{CUT} \ \& \ n_{\text{ch}} = k_{\text{ch}}) \ \text{or} \ (n_{\text{ch}} = \text{CUT} \ \& \ m_{\text{ch}} = k_{\text{ch}}) \right\} \right\} \end{aligned} \quad (57)$$

It is worth mentioning that parameters f_1^* , f_2^* , L_1 and L_2 are functions of $(m_{\text{ch}}, n_{\text{ch}}, k_{\text{ch}})$ and this functionality is eliminated for the sake of brevity in Eq. (56). In other words, for each triple of $(m_{\text{ch}}, n_{\text{ch}}, k_{\text{ch}})$, the parameters f_1^* , f_2^* , L_1 and L_2 are calculated by Eqs. (27)–(53) in Appendix A. Inserting Eq. (54) in Eq. (56) we have:

$$\begin{aligned} G_{\text{NLI}}^{(2)}(f_{\text{CUT}}) &\cong \frac{16}{27} \times \sum_{(m_{\text{ch}}, n_{\text{ch}}, k_{\text{ch}}) \in S'_2} G_{m_{\text{ch}}} \times G_{n_{\text{ch}}} \times G_{k_{\text{ch}}} \times \\ &\sum_{n_s=1}^{N_s} \gamma_{n_s}^2 \times \prod_{p=1}^{(n_s-1)} \Gamma_p(f_{c,m_{\text{ch}}}) \Gamma_p(f_{c,n_{\text{ch}}}) \Gamma_p(f_{k_{\text{ch}}}) A_p(f_{c,m_{\text{ch}}}) A_p(f_{c,n_{\text{ch}}}) A_p(f_{c,k_{\text{ch}}}) \\ &\times \prod_{p=n_s}^{N_s} \Gamma_p(f_{\text{CUT}}) A_p(f_{\text{CUT}}) \times \\ &\int_{f_1^* - L_1/2}^{f_1^* + L_1/2} \int_{f_2^* - L_2/2}^{f_2^* + L_2/2} \frac{df_2 df_1}{4 \left[\alpha_{(m_{\text{ch}}, n_{\text{ch}}, k_{\text{ch}})}^{(n_s)} \right]^2 + 16\pi^4 (f_1 - f_{\text{CUT}})^2 (f_2 - f_{\text{CUT}})^2 \times [\beta_{2,n_s} + \pi\beta_{3,n_s} (f_1 + f_2 - 2f_{n_s}^c)]^2} \end{aligned} \quad (58)$$

$G_{m_{\text{ch}}}$ in Eq. (58) is the PSD of the m_{ch} -th channel at the launch point ($z = 0$ in first span). The PSD at the input of n_s -th fiber span is:

$$G_{m_{\text{ch}}}^{(n_s)} \triangleq G_{m_{\text{ch}}} \times \prod_{p=1}^{(n_s-1)} \Gamma_p(f_{c,m_{\text{ch}}}) A_p(f_{c,m_{\text{ch}}}) \quad (59)$$

Therefore, using Eq. (59), Eq. (58) can be also represented as:

$$G_{\text{NLI}}^{(2)}(f_{\text{CUT}}) \cong \frac{16}{27} \times \sum_{n_s=1}^{N_s} \gamma_{n_s}^2 \times \sum_{(m_{\text{ch}}, n_{\text{ch}}, k_{\text{ch}}) \in S_2'} G_{m_{\text{ch}}}^{(n_s)} \times G_{n_{\text{ch}}}^{(n_s)} \times G_{k_{\text{ch}}}^{(n_s)} \times \prod_{p=n_s}^{N_s} \Gamma_p(f_{\text{CUT}}) A_p(f_{\text{CUT}}) \times \int_{f_1^*-L_1/2}^{f_1^*+L_1/2} \int_{f_2^*-L_2/2}^{f_2^*+L_2/2} \frac{df_2 df_1}{4 \left[\alpha_{(m_{\text{ch}}, n_{\text{ch}}, k_{\text{ch}})}^{(n_s)} \right]^2 + 16\pi^4 (f_1 - f_{\text{CUT}})^2 (f_2 - f_{\text{CUT}})^2 \times [\beta_{2, n_s} + \pi \beta_{3, n_s} (f_1 + f_2 - 2f_{n_s}^c)]^2} \quad (60)$$

To have an analytic solution for the double integral in Eq. (60), we approximately replace the term $\beta_{2, n_s} + \pi \beta_{3, n_s} (f_1 + f_2 - 2f_{n_s}^c)$ with its value at the center of the equivalent rectangular island similar to the approaches in [9,10]. We define:

$$\beta_{2, \text{eff}, m_{\text{ch}}, n_{\text{ch}}, k_{\text{ch}}}^{(n_s)} \triangleq \beta_{2, n_s} + \pi \beta_{3, n_s} (f_1^* + f_2^* - 2f_{n_s}^c) \quad (61)$$

Therefore Eq. (60) can be approximately written as:

$$G_{\text{NLI}}^{(2)}(f_{\text{CUT}}) \cong \frac{16}{27} \times \sum_{n_s=1}^{N_s} \gamma_{n_s}^2 \times \sum_{(m_{\text{ch}}, n_{\text{ch}}, k_{\text{ch}}) \in S_2'} G_{m_{\text{ch}}}^{(n_s)} \times G_{n_{\text{ch}}}^{(n_s)} \times G_{k_{\text{ch}}}^{(n_s)} \times \prod_{p=n_s}^{N_s} \Gamma_p(f_{\text{CUT}}) A_p(f_{\text{CUT}}) \times \int_{f_1^*-L_1/2}^{f_1^*+L_1/2} \int_{f_2^*-L_2/2}^{f_2^*+L_2/2} \frac{df_2 df_1}{4 \left[\alpha_{(m_{\text{ch}}, n_{\text{ch}}, k_{\text{ch}})}^{(n_s)} \right]^2 + 16\pi^4 (f_1 - f_{\text{CUT}})^2 (f_2 - f_{\text{CUT}})^2 \times [\beta_{2, \text{eff}, m_{\text{ch}}, n_{\text{ch}}, k_{\text{ch}}}^{(n_s)}]^2} \quad (62)$$

Changing the variables of the double integral to $f_1' = f_1 - f_{\text{CUT}}$ and $f_2' = f_2 - f_{\text{CUT}}$, we can rewrite Eq. (62) as:

$$G_{\text{NLI}}^{(2)}(f_{\text{CUT}}) \cong \frac{16}{27} \times \sum_{n_s=1}^{N_s} \gamma_{n_s}^2 \times \sum_{(m_{\text{ch}}, n_{\text{ch}}, k_{\text{ch}}) \in S_2'} G_{m_{\text{ch}}}^{(n_s)} \times G_{n_{\text{ch}}}^{(n_s)} \times G_{k_{\text{ch}}}^{(n_s)} \times \prod_{p=n_s}^{N_s} \Gamma_p(f_{\text{CUT}}) A_p(f_{\text{CUT}}) \times \int_{f_1' - f_{\text{CUT}} - L_1/2}^{f_1' - f_{\text{CUT}} + L_1/2} \int_{f_2' - f_{\text{CUT}} - L_2/2}^{f_2' - f_{\text{CUT}} + L_2/2} \frac{df_2' df_1'}{4 \left[\alpha_{(m_{\text{ch}}, n_{\text{ch}}, k_{\text{ch}})}^{(n_s)} \right]^2 + 16\pi^4 f_1'^2 f_2'^2 \times [\beta_{2, \text{eff}, m_{\text{ch}}, n_{\text{ch}}, k_{\text{ch}}}^{(n_s)}]^2} \quad (63)$$

The double integral in Eq. (63) has an obvious solution of $(L_1 \times L_2) / \left(4 \left[\alpha_{(m_{\text{ch}}, n_{\text{ch}}, k_{\text{ch}})}^{(n_s)} \right]^2 \right)$ when $|\beta_{2, \text{eff}, m_{\text{ch}}, n_{\text{ch}}, k_{\text{ch}}}^{(n_s)}| = 0$ while for $|\beta_{2, \text{eff}, m_{\text{ch}}, n_{\text{ch}}, k_{\text{ch}}}^{(n_s)}| \neq 0$ it has also a more complex analytic solution

and we can write:

$$\begin{aligned}
 G_{\text{NLI}}^{(2)}(f_{\text{CUT}}) &\cong \frac{16}{27} \times \sum_{n_s=1}^{N_s} \gamma_{n_s}^2 \times \sum_{(m_{\text{ch}}, n_{\text{ch}}, k_{\text{ch}}) \in S_2'} G_{m_{\text{ch}}}^{(n_s)} \times G_{n_{\text{ch}}}^{(n_s)} \times G_{k_{\text{ch}}}^{(n_s)} \times \\
 &\prod_{p=n_s}^{N_s} \Gamma_p(f_{\text{CUT}}) A_p(f_{\text{CUT}}) \times \\
 &\frac{1}{16 \times \pi^2 \times \alpha_{(m_{\text{ch}}, n_{\text{ch}}, k_{\text{ch}})}^{(n_s)} \times \left| \beta_{2, \text{eff}, m_{\text{ch}}, n_{\text{ch}}, k_{\text{ch}}}^{(n_s)} \right|} \times \\
 &\left\{ F_{\text{int}} \left(\frac{2\pi^2 \times \left| \beta_{2, \text{eff}, m_{\text{ch}}, n_{\text{ch}}, k_{\text{ch}}}^{(n_s)} \right|}{\alpha_{(m_{\text{ch}}, n_{\text{ch}}, k_{\text{ch}})}^{(n_s)}} \times (f_2^* - f_{\text{CUT}} + L_2/2) \times (f_1^* - f_{\text{CUT}} + L_1/2) \right) + \right. \\
 &F_{\text{int}} \left(\frac{2\pi^2 \times \left| \beta_{2, \text{eff}, m_{\text{ch}}, n_{\text{ch}}, k_{\text{ch}}}^{(n_s)} \right|}{\alpha_{(m_{\text{ch}}, n_{\text{ch}}, k_{\text{ch}})}^{(n_s)}} \times (f_2^* - f_{\text{CUT}} - L_2/2) \times (f_1^* - f_{\text{CUT}} - L_1/2) \right) - \\
 &F_{\text{int}} \left(\frac{2\pi^2 \times \left| \beta_{2, \text{eff}, m_{\text{ch}}, n_{\text{ch}}, k_{\text{ch}}}^{(n_s)} \right|}{\alpha_{(m_{\text{ch}}, n_{\text{ch}}, k_{\text{ch}})}^{(n_s)}} \times (f_2^* - f_{\text{CUT}} + L_2/2) \times (f_1^* - f_{\text{CUT}} - L_1/2) \right) - \\
 &\left. F_{\text{int}} \left(\frac{2\pi^2 \times \left| \beta_{2, \text{eff}, m_{\text{ch}}, n_{\text{ch}}, k_{\text{ch}}}^{(n_s)} \right|}{\alpha_{(m_{\text{ch}}, n_{\text{ch}}, k_{\text{ch}})}^{(n_s)}} \times (f_2^* - f_{\text{CUT}} - L_2/2) \times (f_1^* - f_{\text{CUT}} + L_1/2) \right) \right\} \quad (64)
 \end{aligned}$$

The function F_{int} in Eq. (64) is:

$$F_{\text{int}}(x) \triangleq j \times \left\{ Li_2(-jx) - Li_2(jx) \right\} \quad (65)$$

The function $Li_2(x)$ in Eq. (65) is the polylogarithm function or Jonquiere's function of order two that can be approximated by $asinh(\cdot)$ function as [9]:

$$F_{\text{int}}(x) \triangleq j \times \left\{ Li_2(-jx) - Li_2(jx) \right\} \cong \pi \times asinh(x/2) \quad (66)$$

Therefore, using Eq. (66), Eq. (64) can be finally approximated as:

$$\begin{aligned}
 G_{\text{NLI}}^{(2)}(f_{\text{CUT}}) &\cong \frac{16}{27} \times \sum_{n_s=1}^{N_s} \gamma_{n_s}^2 \times \sum_{(m_{\text{ch}}, n_{\text{ch}}, k_{\text{ch}}) \in S_2'} G_{m_{\text{ch}}}^{(n_s)} \times G_{n_{\text{ch}}}^{(n_s)} \times G_{k_{\text{ch}}}^{(n_s)} \times \\
 &\left\{ \prod_{p=n_s}^{N_s} \Gamma_p(f_{\text{CUT}}) A_p(f_{\text{CUT}}) \right\} \times J_{m_{\text{ch}}, n_{\text{ch}}, k_{\text{ch}}}^{(n_s)} \quad (67)
 \end{aligned}$$

Considering the case of $\left| \beta_{2, \text{eff}, m_{\text{ch}}, n_{\text{ch}}, k_{\text{ch}}}^{(n_s)} \right| = 0$, Eq. (64) has a singularity. In this case we can directly calculate the double integration in Eq. (63). Therefore $J_{m_{\text{ch}}, n_{\text{ch}}, k_{\text{ch}}}^{(n_s)}$ in Eq. (67) is:

$$J_{m_{\text{ch}}, n_{\text{ch}}, k_{\text{ch}}}^{(n_s)} = \begin{cases} W_{m_{\text{ch}}, n_{\text{ch}}, k_{\text{ch}}}^{(n_s)} & \text{for } \left| \beta_{2, \text{eff}, m_{\text{ch}}, n_{\text{ch}}, k_{\text{ch}}}^{(n_s)} \right| > 0 \\ \frac{L_1 \times L_2}{4 \left[\alpha_{(m_{\text{ch}}, n_{\text{ch}}, k_{\text{ch}})}^{(n_s)} \right]^2} & \text{for } \left| \beta_{2, \text{eff}, m_{\text{ch}}, n_{\text{ch}}, k_{\text{ch}}}^{(n_s)} \right| = 0 \end{cases} \quad (68)$$

where $W_{m_{ch}, n_{ch}, k_{ch}}^{(n_s)}$ in Eq. (68) is:

$$\begin{aligned}
 W_{m_{ch}, n_{ch}, k_{ch}}^{(n_s)} &= \frac{1}{16 \times \pi \times \alpha_{(m_{ch}, n_{ch}, k_{ch})}^{(n_s)} \times |\beta_{2,eff, m_{ch}, n_{ch}, k_{ch}}^{(n_s)}|} \times \\
 &\left\{ \operatorname{asinh} \left(\frac{\pi^2 \times |\beta_{2,eff, m_{ch}, n_{ch}, k_{ch}}^{(n_s)}|}{\alpha_{(m_{ch}, n_{ch}, k_{ch})}^{(n_s)}} \times (f_2^* - f_{CUT} + L_2/2) \times (f_1^* - f_{CUT} + L_1/2) \right) + \right. \\
 &\operatorname{asinh} \left(\frac{\pi^2 \times |\beta_{2,eff, m_{ch}, n_{ch}, k_{ch}}^{(n_s)}|}{\alpha_{(m_{ch}, n_{ch}, k_{ch})}^{(n_s)}} \times (f_2^* - f_{CUT} - L_2/2) \times (f_1^* - f_{CUT} - L_1/2) \right) - \\
 &\operatorname{asinh} \left(\frac{\pi^2 \times |\beta_{2,eff, m_{ch}, n_{ch}, k_{ch}}^{(n_s)}|}{\alpha_{(m_{ch}, n_{ch}, k_{ch})}^{(n_s)}} \times (f_2^* - f_{CUT} + L_2/2) \times (f_1^* - f_{CUT} - L_1/2) \right) - \\
 &\left. \operatorname{asinh} \left(\frac{\pi^2 \times |\beta_{2,eff, m_{ch}, n_{ch}, k_{ch}}^{(n_s)}|}{\alpha_{(m_{ch}, n_{ch}, k_{ch})}^{(n_s)}} \times (f_2^* - f_{CUT} - L_2/2) \times (f_1^* - f_{CUT} + L_1/2) \right) \right\} \quad (69)
 \end{aligned}$$

We must mention here that as we use the incoherent GN (iGN) model to derive the formula in Eq. (67), in general, the presented approach can be extended for the scenarios where WDM channel scheme can be different span by span. This is applicable for networks with add/drop channel capability in some nodes. In this case, channel under test (CUT) remains the same for all fiber spans while other channels can be different span by span. Therefore, f_1^*, f_2^*, L_1 and L_2 in Eqs. (68) and (69) are not only dependent to m_{ch}, n_{ch}, k_{ch} but also become function of n_s . In other words, f_1^*, f_2^*, L_1 and L_2 must be calculated by Eqs. (27)–(53) in Appendix A for each span separately. To make the aforementioned extension, Eqs. (67), (68), and (69) are exactly the same as presented above considering the fact that f_1^*, f_2^*, L_1 and L_2 are functions of not only m_{ch}, n_{ch}, k_{ch} but also function of n_s and must be calculated for each span separately by Eqs. (27)–(53) in Appendix A. Also, the set S'_2 in Eq. (67), should be modified to $S'_2^{(n_s)}$ as:

$$\begin{aligned}
 S'_2^{(n_s)} &\triangleq \left\{ (m_{ch}, n_{ch}, k_{ch}) \mid m_{ch} \in \mathbb{N} \ \& \ n_{ch} \in \mathbb{N} \ \& \ k_{ch} \in \mathbb{N} \ \& \right. \\
 &1 \leq m_{ch} \leq N_c^{(n_s)} \ \& \ 1 \leq n_{ch} \leq N_c^{(n_s)} \ \& \ 1 \leq k_{ch} \leq N_c^{(n_s)} \\
 &\left. \ \& \ (m_{ch}, n_{ch}, k_{ch}) \notin \left\{ (m_{ch} = CUT \ \& \ n_{ch} = k_{ch}) \ \text{or} \ (n_{ch} = CUT \ \& \ m_{ch} = k_{ch}) \right\} \right\} \quad (70)
 \end{aligned}$$

where $N_c^{(n_s)}$ is the number of channels in WDM comb for the n_s -th span which in general can be different span by span. The modified version of Eq. (67) will be:

$$\begin{aligned}
 G_{NLI}^{(2)}(f_{CUT}) &\cong \frac{16}{27} \times \sum_{n_s=1}^{N_s} \gamma_{n_s}^2 \times \sum_{(m_{ch}, n_{ch}, k_{ch}) \in S'_2^{(n_s)}} G_{m_{ch}}^{(n_s)} \times G_{n_{ch}}^{(n_s)} \times G_{k_{ch}}^{(n_s)} \times \\
 &\left\{ \prod_{p=n_s}^{N_s} \Gamma_p(f_{CUT}) \mathcal{A}_p(f_{CUT}) \right\} \times J_{m_{ch}, n_{ch}, k_{ch}}^{(n_s)} \quad (71)
 \end{aligned}$$

where $J_{m_{ch}, n_{ch}, k_{ch}}^{(n_s)}$ in Eq. (71) is expressed in Eq. (68) and f_1^*, f_2^*, L_1 and L_2 must be calculated separately for each span through Eqs. (27)–(53) in Appendix A.

Funding. Politecnico di Torino through the PhotoNext initiative; Cisco Systems (SRA OptSys-2020, SRA OptSys-2022).

Disclosures. The authors declare no conflicts of interest.

References

1. A. Mecozzi and R.-J. Essiambre, "Nonlinear shannon limit in pseudolinear coherent systems," *J. Lightwave Technol.* **30**(12), 2011–2024 (2012).
2. R. Dar, M. Feder, A. Mecozzi, and M. Shtaif, "Properties of nonlinear noise in long, dispersion-uncompensated fiber links," *Opt. Express* **21**(22), 25685–25699 (2013).
3. P. Poggiolini, G. Bosco, A. Carena, V. Curri, Y. Jiang, and F. Forghieri, "The gn-model of fiber non-linear propagation and its applications," *J. Lightwave Technol.* **32**(4), 694–721 (2014).
4. A. Carena, G. Bosco, V. Curri, Y. Jiang, P. Poggiolini, and F. Forghieri, "Egn model of non-linear fiber propagation," *Opt. Express* **22**(13), 16335–16362 (2014).
5. P. Serena and A. Bononi, "A time-domain extended gaussian noise model," *J. Lightwave Technol.* **33**(7), 1459–1472 (2015).
6. M. Secondini and E. Forestieri, "Analytical fiber-optic channel model in the presence of cross-phase modulation," *IEEE Photonics Technol. Lett.* **24**(22), 2016–2019 (2012).
7. R. Dar, M. Feder, A. Mecozzi, and M. Shtaif, "Pulse collision picture of inter-channel nonlinear interference in fiber-optic communications," *J. Lightwave Technol.* **34**(2), 593–607 (2016).
8. D. Semrau, R. I. Killey, and P. Bayvel, "Approximation of the gaussian noise model in the presence of inter-channel stimulated raman scattering," www.arXiv.org (2018). Paper arXiv:1808.07940.
9. P. Poggiolini, "A generalized gn-model closed-form formula," arXiv preprint arXiv:1810.06545 (2018).
10. D. Semrau, R. I. Killey, and P. Bayvel, "A closed-form approximation of the gaussian noise model in the presence of inter-channel stimulated raman scattering," *J. Lightwave Technol.* **37**(9), 1924–1936 (2019).
11. D. Semrau, E. Sillekens, R. I. Killey, and P. Bayvel, "A modulation format correction formula for the gaussian noise model in the presence of inter-channel stimulated raman scattering," *J. Lightwave Technol.* **37**(19), 5122–5131 (2019).
12. D. Semrau, L. Galdino, E. Sillekens, D. Lavery, R. I. Killey, and P. Bayvel, "Modulation format dependent, closed-form formula for estimating nonlinear interference in s+ c+ l band systems," in *45th European Conference on Optical Communication (ECOC 2019)*, (IET, 2019), pp. 1–4.
13. M. Ranjbar Zefreh, A. Carena, F. Forghieri, S. Piciaccia, and P. Poggiolini, "Accurate closed-form gn/egn-model formula leveraging a large qam-system test-set," *IEEE Photonics Technol. Lett.* **31**(16), 1381–1384 (2019).
14. M. Ranjbar Zefreh, F. Forghieri, S. Piciaccia, and P. Poggiolini, "Accurate closed-form real-time egn model formula leveraging machine-learning over 8500 thoroughly randomized full c-band systems," *J. Lightwave Technol.* **38**(18), 4987–4999 (2020).
15. M. Ranjbar Zefreh and P. Poggiolini, "A real-time closed-form model for nonlinearity modeling in ultra-wide-band optical fiber links accounting for inter-channel stimulated raman scattering and co-propagating raman amplification," www.arXiv.org (2020). Paper arXiv:2006.03088.
16. P. Poggiolini, "The gn model of non-linear propagation in uncompensated coherent optical systems," *J. Lightwave Technol.* **30**(24), 3857–3879 (2012).
17. A. Alvarado, E. Agrell, D. Lavery, R. Maher, and P. Bayvel, "Replacing the soft-decision fec limit paradigm in the design of optical communication systems," *J. Lightwave Technol.* **33**(20), 4338–4352 (2015).
18. P. Poggiolini, A. Carena, Y. Jiang, G. Bosco, V. Curri, and F. Forghieri, "Impact of low-osnr operation on the performance of advanced coherent optical transmission systems," in *2014 The European Conference on Optical Communication (ECOC)*, (IEEE, 2014), pp. 1–3).
19. A. Alvarado, T. Fehenberger, B. Chen, and F. M. Willems, "Achievable information rates for fiber optics: Applications and computations," *J. Lightwave Technol.* **36**(2), 424–439 (2018).
20. P. Serena, "Nonlinear signal–noise interaction in optical links with nonlinear equalization," *J. Lightwave Technol.* **34**(6), 1476–1483 (2016).
21. A. Ghazisaeidi, "A theory of nonlinear interactions between signal and amplified spontaneous emission noise in coherent wavelength division multiplexed systems," *J. Lightwave Technol.* **35**(23), 5150–5175 (2017).
22. P. Poggiolini, Y. Jiang, A. Carena, and F. Forghieri, "Analytical modeling of the impact of fiber non-linear propagation on coherent systems and networks," *Enabling Technologies for High Spectral-Efficiency Coherent Optical Communication Networks* pp. 247–309 (2016).
23. P. Davis, R. Vitale, and E. Ben-Sabar, "On the deterministic and stochastic approximation of regions," *J. Approx. Theory* **21**(1), 60–88 (1977).
24. P. Bourke, "Calculating the area and centroid of a polygon," *Swinburne Univ. of Technology* **7** (1988).
25. P. Ghavami, *Mechanics of materials: an introduction to engineering technology* (Springer, 2014).
26. A. Bononi, R. Dar, M. Secondini, P. Serena, and P. Poggiolini, "Fiber Nonlinearity and Optical System Performance," *Springer Handbook of Optical Networks* (Springer, 2020).